SYNTHESIS AND INDENTATION OF BORIDE AND CARBIDE COATED CARBON NANOTUBE COMPOSITE MICROSTRUCTURES

By

CARLY RENEE SANDIN

THESIS

Submitted in partial fulfillment of the requirements
for the degree of Master of Science in Mechanical Engineering
in the Graduate College of the
University of Illinois at Urbana-Champaign, 2016

Urbana, Illinois

Adviser:

Professor Sameh Tawfick

ABSTRACT

The goal of this thesis is to investigate the synthesis and mechanical behavior of novel refractory coatings for applications subjected to extreme conditions. Starting from aligned carbon nanotube (CNT) forests as scaffolds, composite foams are fabricated by infiltration with refractory materials to achieve desirable mechanical properties such as high stiffness and strength. Similar to naturally occurring materials such as bone and teeth, these properties are dictated by the composition and nanoarchitecture of the material structure. CNTs grown into vertically aligned pillars by chemical vapor deposition (CVD) mimic the microstructure of these natural foams through their porous nanostructure. The CNT pillars are then coated using two methods: (i) static CVD with a hafnium diboride precursor ($Hf[BH_4]_4$) leading to coating thicknesses ranging from 3nm to 50 nm; and (ii) through cycles of elasto-capillary imbibition and pyrolysis of a silicon oxycarbide (SiOC) polymer derived ceramic leading to coating thickness from 8 nm to full infiltration. Both coatings enable the infiltration of CNT pillars and lead to a significant increase in stiffness and strength. Nanoindentation tests using a flat punch were performed on the CNT pillars to measure their Young's modulus and compressive strength. By varying the CNT coating thickness, a trend develops for the Young's modulus as a function of coating thickness for the CNT pillars where $E \sim \rho^{1.698}$ for hafnium diboride coated pillars. The maximum stiffness and strength was 56.49 GPa and 1.94 GPa for the fully infiltrated HfB_2 composite and 3.80 GPa and 13.87 MPa for the SiOC pillars. We also identify the different regimes of deformation for the pillars to better understand the coating processes and the material behavior. These results can enable new applications of CNTs in extreme environments where high temperature resistance and high mechanical resilience are needed, such as hypersonic vehicles.

To the artist and the dreamer.

ACKNOWLEDGEMENTS

Thank you to my adviser Dr. Sameh Tawfick for your guidance and support throughout my graduate education. I am grateful for your insights, discussions and encouragement that led to the completion of this thesis and my degree.

Thank you to my friends and research group: Matt R., Pingju, Yue, Kaihao, Matt P., Alex and Jonathan. Thank you for sharing your technical expertise and for creating such a friendly and welcoming atmosphere in our group.

I would like to express to my sincere gratitude to our collaborators Tushar Talukdar and Professor John Abelson. This work would not have been possible without the constant communication and support of their work and expertise.

Thank you to the Materials Research Laboratory (MRL) staff for their assistance and guidance in using the instruments. Thank you to Kathy and Hongui for helping me improve my instrumentation skills critical to completing this work.

I would also like to thank the University of Illinois at Urbana-Champaign, especially the Mechanical Engineering Department for supporting students and their academic goals. Thank you to all the faculty and staff that I had an opportunity to interact with in class or through my teaching assistantships.

Thank you to my family and friends for your encouragement and friendship throughout my pursuits in life. Thank you to my husband Seth Kijewski for your love and support of my dreams. You are always there for me and I am so grateful for you.

Thank you God, for giving me the strength to do the things I doubted I could.

TABLE OF CONTENTS

CHAPTER 1: INTRODUCTION 1

1.1. Introduction 1

1.2. Bioinspired Materials 1

1.3. Carbon Nanotubes 1

1.4. CNT Composite Foams 2

1.5. Need for Advanced Materials 3

1.6. Thesis Outline 3

CHAPTER 2: LITERATURE 4

2.1. Introduction 4

2.2. Terminology 4

2.2.1. Sample Geometry 4

2.2.2. CNT Types 6

2.2.3. Coating Materials 6

2.2.4. Coating Processes 7

2.2.5. Reported Properties 8

2.3. CNT Composites 8

2.4. Coated CNT Modeling 12

2.5. Polymer Derived Ceramic Coatings 14

CHAPTER 3: EXPERIMENTAL PROCEDURES 16

3.1. Introduction 16

3.2. Starting Materials and Methods 16

3.3. High Temperature Ceramic Coatings 25

3.3.1. Hafnium Diboride Coating 25

3.3.2. Polymer Derived Ceramic Coating 29

3.4. Nanoindenter Instrument 31

3.5. Nanoindentation Testing 34

CHAPTER 4: RESULTS 36
4.1. Introduction 36
4.2. Stress-Strain Plots for Uncoated Pillars 36
4.3. Stress-Strain Plots for HfB_2 Coated Pillars 38
4.4. Stress-Strain Plots for PDC Pillars 51
CHAPTER 5: DISCUSSION 60
5.1. Introduction 60
5.2. Young's Modulus as a Function of Coating Thickness 60
5.3. Strength as a Function of Coating Thickness 65
CHAPTER 6: CONCLUSIONS AND RECOMMENDATIONS 67
6.1. Overview 67
6.2. Conclusions 67
6.3. Recommendations for Future Work 68
REFERENCES 70
APPENDIX A: STAGE TO TIP CALIBRATION 72
APPENDIX B: SAMPLE NAVIGATION 73

CHAPTER 1: INTRODUCTION

1.1. Introduction

The overarching goal of this thesis is to design, synthesize and test nano-architectured materials for extreme environments requiring damage tolerance at high temperatures. As a first step towards this goal, the synthesis and mechanical behavior of nano-composites made from aligned carbon nanotube (CNT) pillars coated with different types of refractory materials was investigated.

1.2. Bioinspired Materials

The materials studied in this thesis are inspired by damage tolerant natural materials. Many natural materials are composed of multiple constituents arranged in a complex hierarchical architecture [1]. The resulting materials are lightweight composites that display unique property combinations. Bone, tooth, bamboo and nacre (abalone shell) are all examples of naturally occurring lightweight composites that exhibit high strength, high toughness and damage-tolerance [1]. These properties are driven by the composition and orientation of the constituents at the nanoscale level [2].

The features and structural mechanisms of these natural materials have been difficult to replicate [3]. There is a lack of accessible and adequate processing techniques for artificial materials able to mimic the advanced structural layering at the micro and nanoscale levels [4]. Recent work has identified additive manufacturing as one platform to manufacture complex-shaped parts modeled after bioinspired heterogeneous microstructures [4]. One example is reinforcing a polymer matrix using particles or metal platelets [5]. These platelet-reinforced polymers display remarkable mechanical properties in comparison to natural materials and the technique allows for local modification of the assembly, concentration, and orientation of the particles [5].

1.3. Carbon Nanotubes

Carbon nanotubes (CNTs) are tubular-structured materials consisting of a thin layer of graphite. The diameter of a CNT is on the nanoscale level while the length varies based on growth conditions. The unique electronic, magnetic and mechanical properties in combination with their size is what makes CNTs an extraordinary material. Though the intrinsic properties of individual CNTs are desirable, further processing is required to make CNTs into a functional, manufactural material. One method used to advance CNTs towards this goal is material deposition, or coating. Coating CNTs improves the strength and stiffness of individual CNTs as well as a bulk material. In this thesis, coated CNT materials are called CNT composite foams.

1.4. CNT Composite Foams

CNTs can mimic the porous structure of foam materials when grown from defined catalyst areas. Individual CNTs within the catalyst area grow vertically and contact neighboring CNTs forming a CNT network or forest. The contacting CNTs form open spaces, like the pores or cells of a typical foam. Van der Waals forces hold these connection points in place forming bonds within the CNT network. However, these bonds are weak under compressive loading for uncoated CNTs. This is where the CNT material can be improved using novel methods. Conformal coating of CNT forests increases the stiffness and strength of individual CNTs and creates strong coated CNT junctions [6]. Coating deposition can be done through methods like chemical vapor deposition (CVD) or spin-coating. The porous characteristic of CNT foams allows the coating material to infiltrate through the cells and conformally coat the CNT surfaces, including interior CNTs. This makes CNTs an attractive template for creating composite materials.

Ultra-High-Temperature Materials

The overall properties of these new CNT composite foams are dependent upon the coating material properties. In ceramics, there is a small number of elements or compounds that have melting temperatures exceeding 3000 ℃ [7]. Ultra-high-temperature ceramics (UHTCs) is a class of materials with melting temperatures above 3000 ℃ and suitable for applications above 2000 ℃. Leading edges and nose tips on reentry vehicles are two examples of areas that are subjected to temperatures exceeding 2000 ℃ [8], [9].

Zirconium diboride (ZrB_2) and hafnium diboride (HfB_2) are two examples of ultra-high temperature refractory metals that have high melting temperatures, high electrical and thermal conductivities, good resistance to corrosion and are chemically stable making them suitable for extreme environments like hypersonic flight [7]. The high melting temperatures of these materials makes them difficult to be cast or machined easily and creates challenges for additive manufacturing techniques [10]. CVD is an alternative method to creating solid ceramic materials without needing to reach the high melting point.

Chemical Vapor Deposition.

Chemical vapor deposition (CVD) is typically used to create thin films and coatings. Instead of solid materials, CVD uses gas phases of materials called precursors and heat to generate chemical reactions. The chemical reaction deposits a thin layer of solid material over the substrate or base material. CVD is a desirable method because processing can be done at low temperatures. However, CVD is reaction limited. The deposition thickness does not reach beyond the nanometer range. Using

CVD to coat a solid surface limits the coating to a thin layer whereas coating a porous material allows the precursor to infiltrate through the material and coat surfaces within the cells. In this way, coating a CNT foam creates a thick material by infiltration.

1.5. Need for Advanced Materials

There is a need for advanced materials as technology is used to explore and operate in extreme environments. In aerodynamics, hypersonic flight refers to vehicles flying at speeds of Mach 5 and above. Aerodynamic friction at these speeds presents challenges for designers. Surface temperatures, surface pressures, and oxidation all become critical factors at hypersonic speeds. Materials must be able to withstand extreme conditions while maintaining performance. To combat these challenges, parts are created using materials that have extremely high melting temperatures. Standard methods used to forge these materials require extreme processing at the material's melting temperature. There is a need for simpler methods to create advanced materials efficiently. Two examples of potential applications for hypersonic flight and advanced materials are leading edges and heat shields.

1.6. Thesis Outline

The scope of this research includes the synthesis and testing of coated CNT micropillars and a fundamental understanding of CNT micropillar compression by nanoindentation. The two high temperature coatings discussed in this paper are hafnium diboride (HfB_2) by CVD and silicon oxycarbide (SiOC) by spin-coating and pyrolysis. By studying the mechanical properties of CNT composite foams, we can better understand how they can be used in extreme conditions.

Chapter 2 discusses the literature of previous studies on coated CNTs.

Chapter 3 provides the experimental procedures for the design, synthesis, coating and testing of HfB_2 and SiOC coated CNT micropillars.

In Chapter 4, the results and observations of nanoindentation compression testing are reported for the CNT micropillars at various coating thicknesses.

Chapter 5 discusses the trends in the stiffness and compressive strength of the CNT micropillars as a function of coating thickness. This chapter also provides the criterion for the stiffness and strength from the stress-strain curves.

Chapter 6 draws final conclusions and outlines future directions.

CHAPTER 2: LITERATURE

2.1. Introduction

Previous studies have demonstrated how coating carbon nanotube (CNT) pillars enhances the material properties and increases the array of target applications for CNT composite foams. This chapter discusses the results from several studies of different coating materials and methods used to create CNT composite foams. A summary of the studies is presented in Table 2.1. The terms and concepts referenced in these studies are defined and discussed in section 2.2. This chapter also builds a foundation for understanding how CNT composite foams can be modeled as a bulk material.

Table 2.1 Aligned CNT composite foams.

Sample Geometry and Dimensions	CNT Type and Size	Coating Material	Coating Thicknesses	Coating Process	Reported Properties	Reference
Micropillars radius: 10-35 µm height: ~30 µm	MWNT, ~ 10 nm diameter	Alumina	8.5-51 nm	ALD	Modulus, Strength	Brieland-Shoultz [2]
Micropillars, diameter: 5-150 µm height: 100 µm	MWNT, ~ 9 nm diameter	Amorphous Silicon-Carbide	5.6-52 nm	LPCVD	Strength	Poelma [6]
Micropillars, diameter: 10-100 µm height: 100 µm	MWNT, ~ 9 nm diameter	Amorphous Silicon-Carbide	2-30 nm	LPCVD	Modulus, Strength	Poelma [11]

2.2. Terminology

2.2.1. Sample Geometry

CNTs can be grown into a variety of geometries using a defined metal catalyst. The process used to create and sputter a catalyst onto a substrate is explained in detail in Chapter 3. In chemical vapor deposition (CVD), a hydrocarbon gas flows over the catalyst and a chemical reaction causes the carbon molecules to create vertically aligned CNTs within the catalyst area. Thus, the catalyst area acts as the initiation site for CNT growth. In many studies, the catalyst geometry is a circle with a diameter on the microscale level. When the CNTs grow vertically on these circle catalysts they form CNT micropillars. The circles are typically repeated across the substrate to produce rows and columns of CNT pillars. Other shaped-pillars and larger-sized geometry catalysts have also been coated [12].

The catalyst size and geometry is dependent on the study. The terms CNT forest and CNT array are also commonly used to describe CNT growth.

CNT Micropillars

CNT micropillars are favorable for fundamental mechanical measurements because of their size for coating and compression testing. Spacing between the micropillars allows the gas precursors to more easily infiltrate the interior CNTs because there is less bulk CNT material for the precursors to pass through and coat. Isolating the CNT growth into this specific geometry also removes the forces of the bulk material around the tip during nanoindentation testing. Finally, the length to diameter ratio is significant in micropillar testing. The aim for the dimensions of micropillars tested in this study was a 1:1 length to diameter ratio.

CNT Forests

CNT forest is an all-encompassing term to describe the organization of vertically-aligned CNT growth. It is typically used to reference bulk CNT growth (i.e. from non-patterned catalyst) but it is also used to describe the CNT growth within a CNT micropillar. The size of a CNT forest is significant during subsequent CVD coating because of the amount of CNT surface area exposed. As the size of a CNT forest increases, so does the amount of surface area. Samples that have more surface area will consume more of the gas precursors at the same CVD settings, resulting in a thinner coating.

CNT Arrays

The term CNT array is used to describe CNT pillars or CNT forests of defined catalyst areas [6]. Pillar geometry or size for CNT arrays may vary within a sample. In some studies, a range of micropillar sizes are used within the same sample [2], [6].

Tip Dimensions

A tip is used in nanoindentation compression testing to indent or compress CNT samples. Two common tips used in these studies are the Berkovich tip and a flat-punch tip. The Berkovich tip is a three-sided pyramid that indents the surface of a material. A flat-punch tip is used to compress a material. The flat-punch is typically used for testing micropillars and the diameter of the tip is generally slightly larger than the micropillar diameter.

2.2.2. CNT Types

There are many types of CNTs but most are categorized as either single-walled nanotubes (SWNT) or multi-walled nanotubes (MWNT). The ‘c’ in CNT is typically omitted in these terms. The prefix refers to how many layers of graphite or graphene are in the diameter of the nanotube.

SWNTs are conceptually thought of as a single layer of graphite rolled up into a tube. However, they are created from individual carbon molecules forming a nanostructure from an allotrope of carbon. MWNT have multiple graphene layers and can be thought of as concentric cylinders stacked inside one another. The number of layers can vary and the diameter is typically greater than SWNTs.

2.2.3. Coating Materials

The porous template of CNT micropillars allows for a variety of coating materials and methods to coat and infiltrate the pillars. Ceramics are commonly used for coating CNTs. Examples include alumina oxide (Al_2O_3) and silicon carbide (Si-C). Ceramics typically have good strength to weight ratios, high melting and oxidation temperatures and good wear resistance.

Table 2.2 Material properties of ceramic coatings.

Coating Material	**Density**	**Melting Temperature**	**Young’s Modulus**	**Compressive Strength**	**Wear Resistance**
Alumina Oxide (Al_2O_3)	3.95 g/m^3	2,072 °C	215 GPa	2600 MPa	Good
Silicon Carbide (Si-C)	3.21 g/m^3	2,730 °C	137 GPa	1395 MPa	Excellent
Hafnium Diboride (HfB_2)	10.5 g/cm3	3,250 °C	500 GPa	*Hardness 29 GPa	Excellent

Alumina Oxide

Al_2O_3, also called alumina, is a high performance ceramic material that has excellent dielectric properties and high stiffness and strength. Its properties make it a desirable material for electrical resistance and high temperature applications like electrical insulators and furnace liners. Several studies have used Al_2O_3 to coat CNTs [2], [13], [14].

Silicon Carbide

Another material used in coating CNTs is Si-C. Si-C is typically used an abrasive material and has a high melting temperature, robustness, and electrical conductivity [6]. Sintering is a common method used to produce hard ceramics of Si-C. Sintering is the process of compacting or bonding grains together using high heat or pressure.

Hafnium Diboride

Hafnium diboride (HfB_2) is in an ultra-high temperature refractory metal. HfB_2 has an extremely high melting temperature, greater than Al_2O_3 and Si-C (Table 2.1). It also has high electrical conductivity. Sintering and hot pressing are often used to form HfB_2 ceramics. Hot pressing is similar to sintering and uses heat and pressure to compress powder into a solid material.

2.2.4. Coating Processes

The porous nature of CNTs allows researchers to use methods such as chemical vapor deposition (CVD) to infiltrate and uniformly coat CNTs throughout a sample. There are many types of CVD techniques that use different pressures and processes to initiate chemical reactions. Spin-coating is another coating method used to infiltrate CNT micropillars.

Chemical Vapor Deposition

CVD is a deposition technique that uses gas phases of materials called precursors to deposit thin layers of solid materials. A chemical reaction occurs thermally when the molecular species are released in a chamber. The chemical reactions limit the thickness of the film created.

Atomic Layer Deposition

ALD is a subset technique of CVD. ALD also uses precursors to deposit a thin film of coating over the sample. ALD differs by using the precursors sequentially whereas CVD releases the gas phases all at once. This causes the ALD reaction to deposit a single layer of material at a time due to a local interaction at the surface of the coated materials.

Low Pressure Chemical Vapor Deposition

Low pressure CVD (LPCVD) is CVD that operates at sub-atmospheric pressures. The reduced pressured can improve the quality of deposition on a substrate and minimize unwanted reactions.

Spin-coating

Spin-coating can use solid or liquid phases of coating materials. The coating material is usually placed or pipetted onto the center of the sample. Spinning the sample then causes the material to spread over the sample as it radiates outward.

2.2.5. Reported Properties

The reported or measured properties for CNT composite foams vary in the literature. For traditional foams, the young's modulus and compressive strength are important assessments. Melting and oxidation temperature and wear resistance become more important when considering high temperature applications.

Young's Modulus

Young's modulus, used interchangeably with the elastic modulus, is the stress per unit strain in the elastic regime. In a solid material, it is the measure of stiffness. Because of the concentrated stresses during nanoindentation, it is not possible to isolate the elastic response from plastic response during loading (i.e. when the tip is compressing the material). Previous studies have reported the Young's modulus from the loading portion of the curve in nanoindentation, but it is now accepted that Young's modulus should be measured during unloading [15].

Compressive Strength

Compressive strength is a material's ability to withstand applied stress under compression without breaking. The deformation behavior for materials varies under compressive loading, so the considerations for the stress limit also vary. With CNT pillars, the compressive strength is defined as the stress limit before pillar buckling (by collapse) or pillar failure (by fracture). Thin coated pillars have a tendency to collapse under compressive loads while thicker coatings tend to fracture.

2.3. CNT Composites

In this section, the studies summarized in Table 2.1 are discussed. Some studies presented a modeling approach which will be highlighted in a later section.

Al_2O_3 Coated Pillars Using ALD

Brieland-Shoultz et al. [2] reported a predictable ~1000-fold increase in Young's Modulus for Al_2O_3 coated CNT composite foams. In Figure 2.1 the CNT composite foams are compared to manufactured structural materials and published materials with similar density ranges. It was found that the compressive modulus and compressive strength of their CNT composite foams is 10 times

greater than that of aluminum foams that are currently in the market. Their work explores the ability to increase the properties of CNT composite foams and model them as a function of coating thickness.

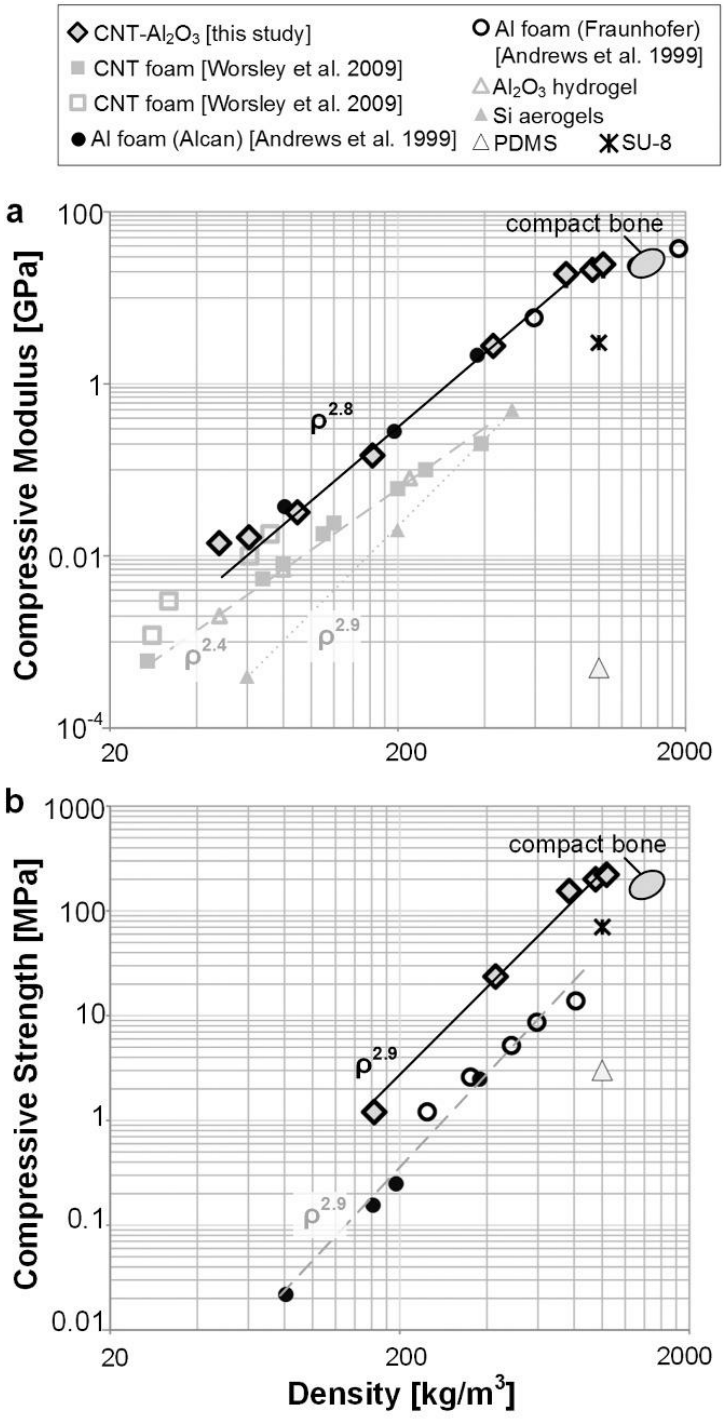

Figure 2.1 Compressive modulus and compressive strength as a function of density for Al_2O_3 coated pillars in comparison to published materials [2].

Various sized CNT micropillars, ranging from 10-25 μm, were coated and tested. The pillars were grown on a metal catalyst of 10 nm Al_2O_3 and 1 nm Fe using CVD and then coated with Al_2O_3 using ALD. The thickness of the Al_2O_3 coating was controlled by the number of ALD cycles. Each cycle of ALD consisted of sequentially adding Al(CH) and H_2O precursors in two half-reaction stages. The initial nucleation of Al_2O_3 occurred at surface defects and contact points between CNTs. After coating formed in these areas, the Al_2O_3 coats over the individual CNTs and bundles of CNTs. A CNT bundle refers to a grouping of CNTs due to Van der Waals forces or proximity of growth. At some point, the coated CNTs coalesce and the gases can no longer reach the interior CNTs. The scanning electron microscope (SEM) images of the coated pillars showed that this coalescence begins at approximately 30 nm of coating and the spacing between in CNTs was confirmed to be smaller than 50 nm.

The pillars were tested in compression using a nanoindenter and a 100 μm diameter flat-punch diamond tip. The pillars were tested using continuous modulus mode at a constant loading of 10 nm oscillations to 2 μm. Load-displacement curves are reported for micropillars with 0, 100 and 1000 ALD cycles of coating corresponding to 0 nm, 13 nm and 51 nm coating. The Young's Modulus was obtained from the unloading slope and reported at 14.5 MPa for uncoated pillars to 24.5 GPa for 51 nm coated pillars.

The coating thickness was found using the average outer radii of uncoated CNTs and comparing the value to the average thickness of the coated CNTs. The relationship between the mass and number of ALD cycles was also determined by using a coated CNT forest. When the precursors are no longer able to diffuse into the CNT forest, the coating has reached coalescence. A model was constructed by incorporating the decreasing pore size from coating and is further explained in Section 2.4.

Silicon Carbide Coated Pillars using CVD

Amorphous silicon carbide (a-SiC) has also been used to coat and strengthen CNT pillars. Si-C is good for applications that require high temperatures, electrical conductivity and wear resistance. Poelma et al. [6] synthesized Si-C coated CNT pillars using CVD. The compressive strength measured by indentation started below 1 MPa for uncoated pillars and increased towards 1.8 GPa for 21.4 nm coated pillars. The increase is by 3 orders of magnitude. The pillar behavior ranged from foam-like failure to particular "bamboo" brittle-like failure.

The low packing density of CNTs and the weak van der Waals forces of the CNT connections are identified as limitations of CNT growth from photolithography defined catalysts. The combination of low density and weak bonds results in CNT pillars that have weaker properties than that of individual

CNTs. Poelma suggests densification and conformal coating are two methods that can be used to overcome these limitations.

The pillar diameters ranged from 5-150 μm with a maximum length to diameter aspect ratio of 10:1. The coating thicknesses reported were 5.6 nm, 10.5 nm, 21.4 nm and 52 nm of Si-C. The thick coated CNT pillars remained somewhat porous which indicated that the precursor gasses could infiltrate the CNT pillar even as the CNTs coalesced. A Berkovich tip and SEM images showed that for every 1 μm of surface penetration into the CNT caused the coating thickness to reduce by 0.14 nm. This value was compared to ellipsometry measurements on flat control samples and showed agreement.

Nanoindentation was performed with a 150 μm diameter flat-punch diamond tip. Continuous stiffness measurement (CSM) mode was used to test the pillars in compression. Uncoated and thinly coated samples collapsed before a plateau region was reached. However, a plateau region was observed in thicker coated samples and it was found that Young's modulus increases with compression depth. The moduli were extracted from the slope of the stress-strain curves before failure occurred. Another observation was the increase in modulus for coated pillars with smaller diameters corresponded to an increase in the depth of compression of the pillars. A gradient in coating thickness of the CNTs in the center of the pillar to the outside of pillar was a possible explanation for the pillar diameter dependency.

The SEM images showed that pillar failure began with localized buckling at the base and propagated vertically up the pillar. In Hutchens et al. [16] study this same localized buckling behavior is observed. Zbib et al. [17] describes the buckling by explaining how CNTs near the base of the pillar reorient themselves laterally under compression causing a folding mechanism to occur in the same direction.

The larger diameter uncoated pillars were compressed to 25%, 20% and 17% of the pillar height and showed 1 or 2 buckling folds while the smaller diameter pillars were compressed at 80% and showed a significant increase in buckling folds, with 9 to 11 folds. The maximum applied stress was determined to be 0.85 MPa before the pillar collapsed, at a compressive strain about 4.8%. The sudden collapse caused an overshoot of the nanoindentation tip towards the substrate because the displacement control feedback could not compensate fast enough. Another issue with uncoated pillars was adhesion to the tip. As a result, uncoated pillars with a diameter less than 60 μm were omitted from the results.

A unique development was observed for pillars with 5.6 nm coating. At this thickness, there were highly aligned vertical cracks and less wrinkles on the outer sides of the pillar. The failure did not start at the base as it had before and there was no typical waveform buckling as was observed in the

uncoated pillars. From the results and observations, it was determined the failure was either matrix failure or a CNT-matrix interface failure. Crack propagation resulting from residual stresses most likely led to this bamboo-splitting failure.

Three regimes of testing were identified for defined strains up to 5%: elastic deformation, small strain burst propagation, and large strain burst propagation. The pillar compressive strength was defined as the maximum applied stress when the first regime transitions into the second regime. The non-periodic buckling was attributed to the second regime while the bamboo-like splitting behavior was attributed to the third regime. A 70% recovery was determined during unloading for all deformed pillars. Furthermore, pillars with 52.0 nm of coating were too strong and could not reach failure due to the maximum load capacity of the nanoindenter instrument.

The uncoated CNT pillar mechanical behavior went from a foam-like material to a bamboo-like failure, typical of fiber reinforced composites. The thicker Si-C coating decreases the distance between coated CNTs resulting in more CNTs that can be bonded together. This increase in coating thickness also increases the mechanical properties. With a conformal coating of about 21.4 nm, the porosity decreased from about 99% to 79% and the bending stiffness increased and the compressive stress increases by about 3 orders of magnitude. Figure 2.2 shows compressive strength results.

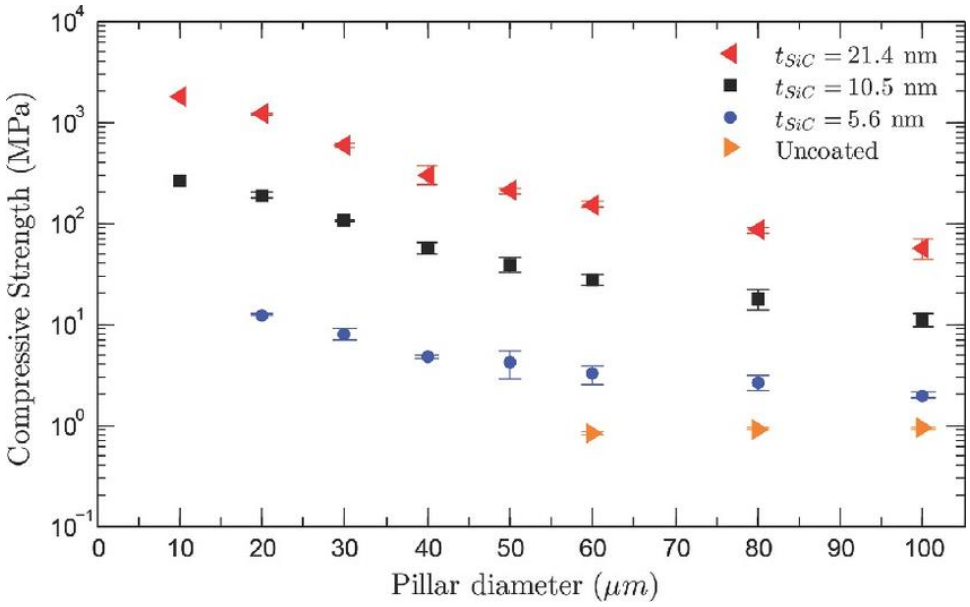

Figure 2.2 Compressive strength as a function of pillar diameter for uncoated and Si-C coated CNT pillars [6].

2.4. Coated CNT Modeling

The work by Brieland-Shoultz et al. [2] presented a model for structural characterization. The uncoated CNTs were compared to open-cell foams where the individual CNTs and CNT bundles

acted like struts. SEM digital image correlation was used to show that the CNT-CNT contact points did not slip when the compressive loading was below a specified failure threshold. The CNT struts were then represented as load-bearing elements that are primarily in bending when the micropillar is loaded in compression. A rectangular unit cell geometry was used created to CNT structure. SAXS determined that the average orientation angle of the individual CNTs relative to the vertical axis was 40°. A unit cell size was calculated for one CNT length, L_{CNT}, to represent the forest structure as shown in a. and b. of Figure 2.3. L_{CNT} was found using stiffness, Young's modulus, the second moment of inertia, area and the measured orientation angle. The first model determined a constant L_{CNT} for the unit cell. However, the experimental results did not align. The model was updated to include a variable L_{CNT} that incorporates the decreasing length of the CNT as the coating increases and aligns nicely with the experimental measurements (c. of Figure 2.3).

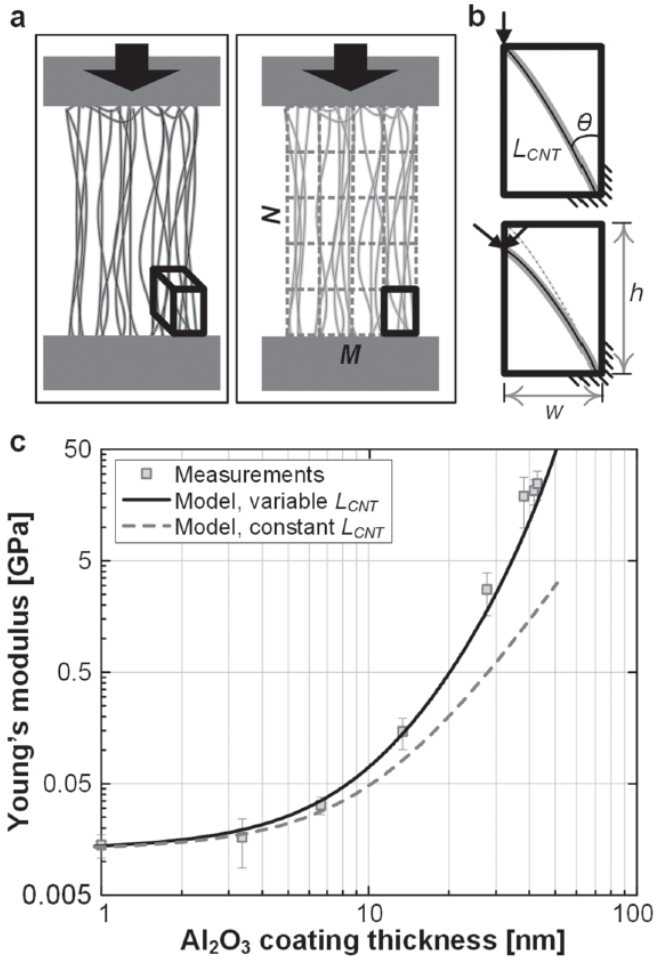

Figure 2.3 Modeling Al_2O_3 coated pillars [2]. a.) Unit cell size for a CNT pillar. b.) An individual CNT "beam" in bending. c.) Model predictions comparing variable and constant CNT lengths with experimental measurements.

Poelma et al. [11] also used a modeling approach to create a unit cell to represent the coated structure and predict experimental. In this model, multiple CNTs were defined in the unit cell as beams. A mesh generation was used to simulate the effect of conformal coating and waviness of CNTs. They determined that the coating thickness increase resulted in an exponential increase for compressive strength and stiffness, matching the results of nanoindentation (Figure 2.4). Poelma suggests a more thorough investigation on van der Waals interactions would benefit the work.

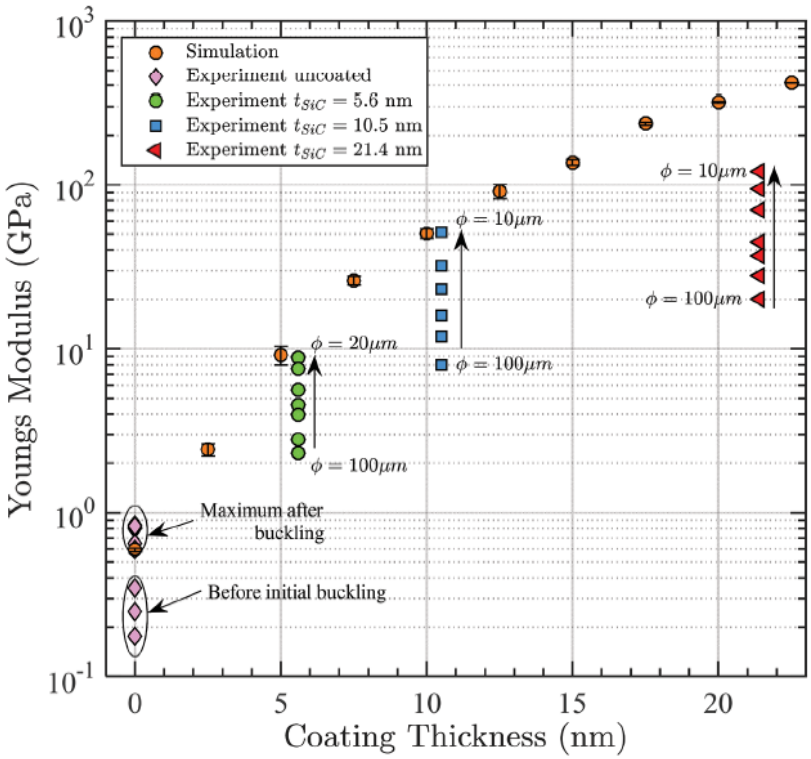

Figure 2.4 Model prediction of the simulation compared to the measurements of the experiment for uncoated and Si-C CNT pillars [11].

2.5. Polymer Derived Ceramic Coatings

Polymer derived ceramic (PDCs) coatings are used in applications that require toughness and heat tolerance. The methods used to manufacture PDC coated materials involve pyrolysis, the decomposition of material using high temperatures. Shah et al. [18] introduces the idea of infiltrating and coating CNTs using PDCs. In Shah's study, a silicon carbonitride (SiCN) coating was used to bond the CNTs in a ceramic-like matrix producing enhanced mechanical robustness. Observations have shown that precursor solutions of PDCs have good wetting with CNTs [19].

Eckel et al. [10] used preceramic monomers cured in ultraviolet (UV) light to create complex shaped and porous three-dimensional (3D) polymer structures. These 3D polymer structures were exposed to pyrolysis and shrunk uniformly into a ceramic. The PDC coated microlattices and honeycomb cellular in this study exhibited higher strengths compared to similar ceramic foams. The structure and composition of the template material determines the resulting structure composition and yield of the PDC material after pyrolysis. To prevent the loss of low-molecular species and fragmentation, high cross-linking in the polymer is needed. The study used a UV-curable siloxane created by mixing methylsiloxane and vinylmethoxysiloxane. A UV-photo initiator was added to the resin to be used in a stereolithography 3D printer. The pyrolysis was a 1000 °C cure in argon resulting in 42% mass loss and 30% linear shrinkage. The silicon oxycarbide (SiOC) ceramic has a has a brittle-like behavior when tested.

CHAPTER 3: EXPERIMENTAL PROCEDURES

3.1. Introduction

This chapter describes the experimental procedures for the design and synthesis of CNT micropillars, the coating of hafnium diboride (HfB_2) and silicon oxycarbide (SiOC) and nanoindentation testing. Photolithography was used to design and produce the defined catalyst areas. Chemical vapor deposition (CVD) was used to grow the vertically aligned CNT micropillars. Two coating methods, CVD and spin-coating, were used to infiltrate the pillars with the coating materials. Nanoindentation was used to perform compression testing on the pillars to determine mechanical properties. The CNTs and pillars were imaged using scanning electron microscopy (SEM).

3.2. Starting Materials and Methods

In this study, CNT growth begins with a metal catalyst deposited onto a substrate. The substrate used in this study is a silicon wafer with a (100) orientation. The catalyst pattern is produced through several steps of photolithography and acts as the starting point for CNT growth. Several different sizes and geometries of micropillars were used.

Photolithography of Catalysts

Photolithography is a process used to pattern a substrate using chemical treatments and the transfer of light. A light-sensitive chemical called photoresist (SPR220) is deposited onto a silicon wafer using spin-coating and a photomask transfers the sample pattern onto the coated wafer. The photomask is an opaque plate that contains a pattern of transparent holes or shapes. In this study, the photomask was a chrome soda lime mask manufactured by Photomask Services at Frederick Seitz Materials Research Laboratory and can be seen in Figure 3.1. UV light shines through the photomask and the transparent pattern is transferred onto the coated substrate. After the pattern is transferred, the entire silicon wafer is developed to expose the catalyst pattern. Finally, a sequence of sputtering deposits the metal catalyst onto the silicon wafer. The sputtering sequence is 20 nm of alumina oxide (Al_2O_3) and then 1 nm of iron (Fe).

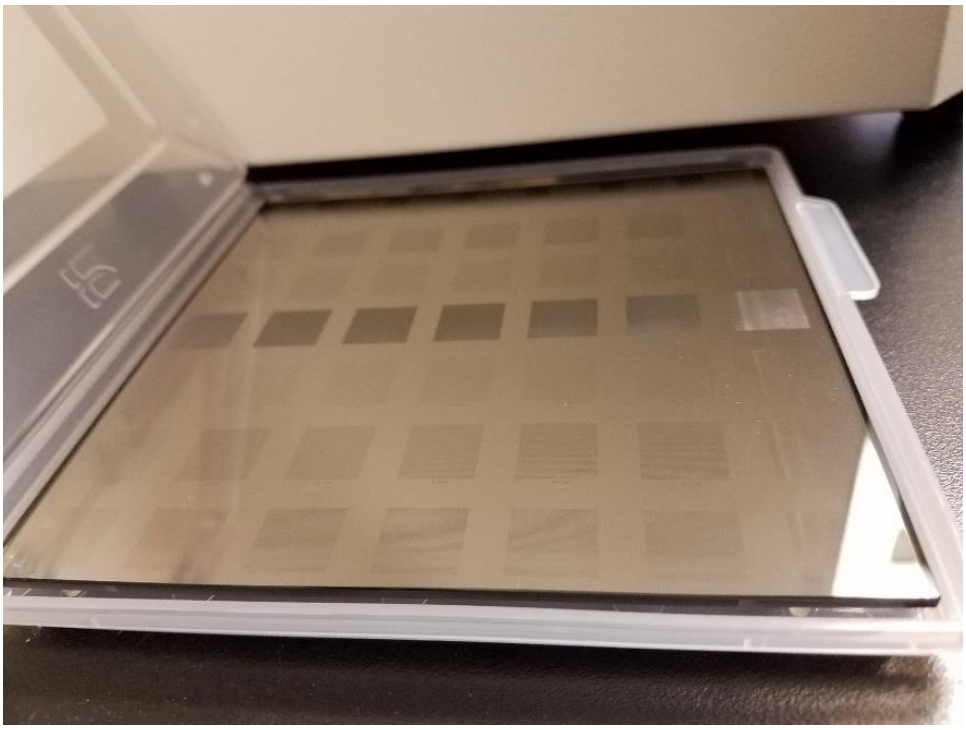

Figure 3.1 Chrome soda lime photomask with various transparent sample patterns.

Micropillar Geometries

Rectangular and octagonal micropillars were used to study the mechanical behavior of CNT composite foams. Catalyst dimensions and a representative SEM image of each pillar's cross section are listed in Table 3.1. The images were taken with a Hitachi S-4800 SEM as shown in Figure 3.2. The pillars are referred to by their geometry and size as Rectangle Pillar, Octagon Pillar - 100, Octagon Pillar - 50 and Octagon Pillar - 25. The Rectangle Pillars all have a catalyst dimension of approximately 30 µm by 60 µm. The Octagon Pillars are referenced by their approximate "diameter" of 100 µm, 50 µm and 25 µm. This diameter is the largest diagonal of the octagon, from end point to end point, as shown in Figure 3.3.

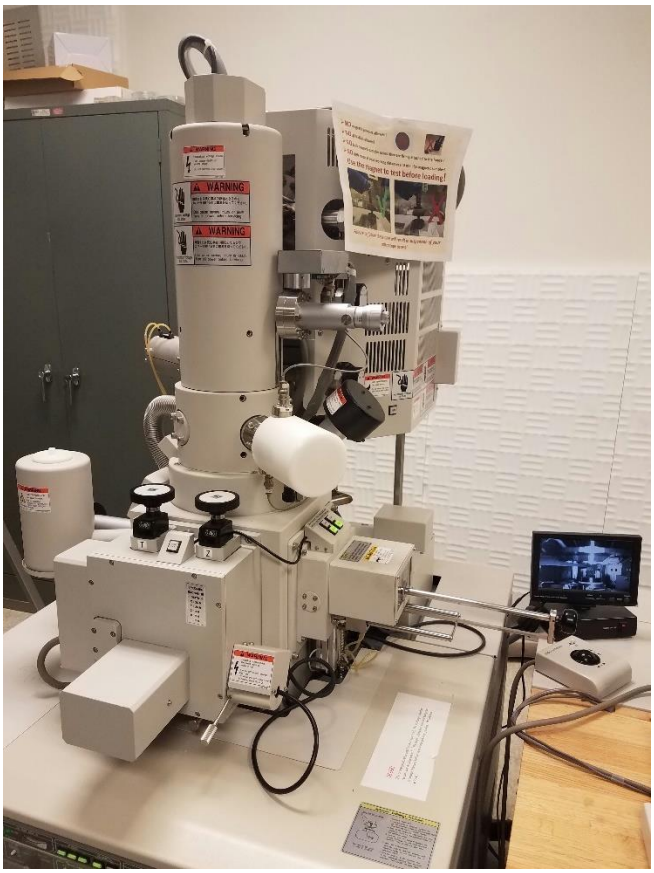

Figure 3.2 Hitachi S-4800 scanning electron microscope (SEM).

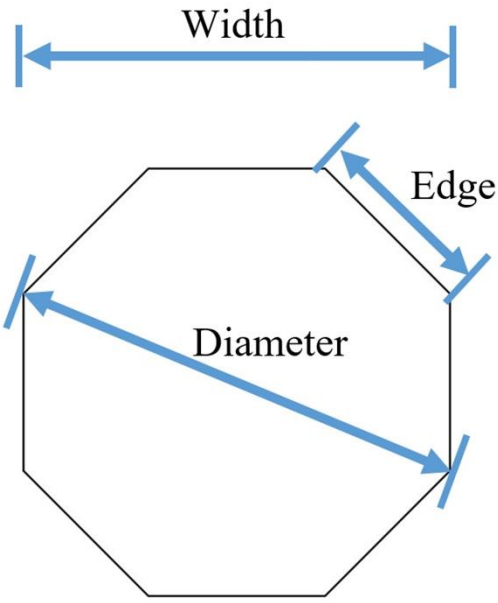

Figure 3.3 Dimensional reference for the octagon pillars.

The first micropillars used in this study were the Rectangle Pillars. The switch to the Octagon Pillars was made to more closely resemble the nanoindentation tip geometry shown Figure 3.11. Initially, the new pattern was designed to be circles. However, the photomask pattern was limited by the amount of data that the manufacturing equipment could receive, so octagons were used instead to optimize the number of pillars within each sample.

Table 3.1 Sample geometries for CNT micropillars.

Micropillar Name	**Catalyst Dimensions**	**SEM Image – View of Micropillar Cross Section** *50µm scale
Rectangle Pillar	Rectangle Width: 30 µm Height: 60 µm Area: 1800 µm^2	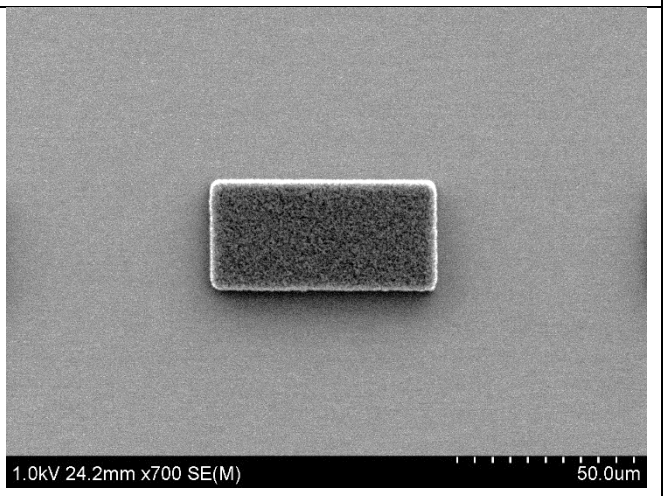
Octagon Pillar - 100	Octagon Diameter: 100 µm Edge: 19.13 µm Area: 7071.10 µm^2	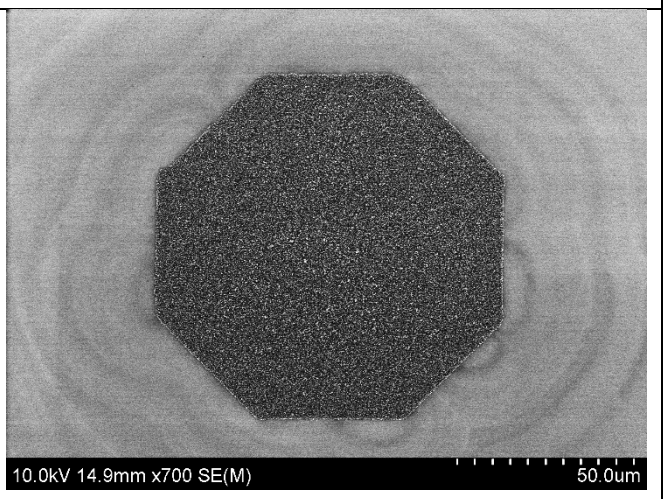

Table 3.1 (cont.)

Octagon Pillar - 50	Octagon Diameter: 50 µm Edge: 38.27 µm Area: 1767.77 µm^2	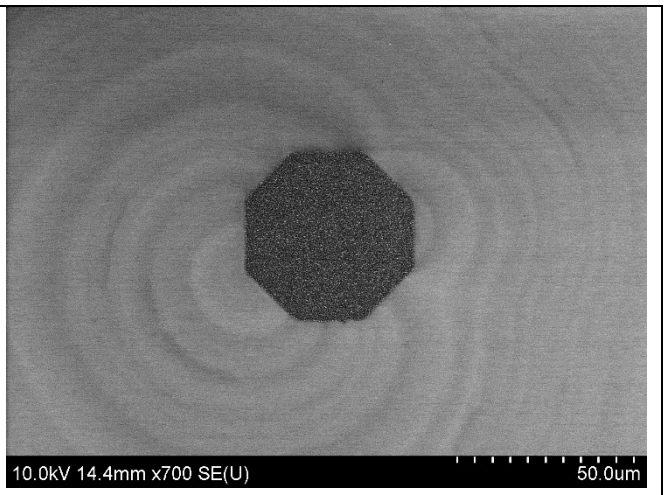
Octagon Pillar - 25	Octagon Diameter: 25 µm Edge: 9.57 µm Area: 441.94 µm^2	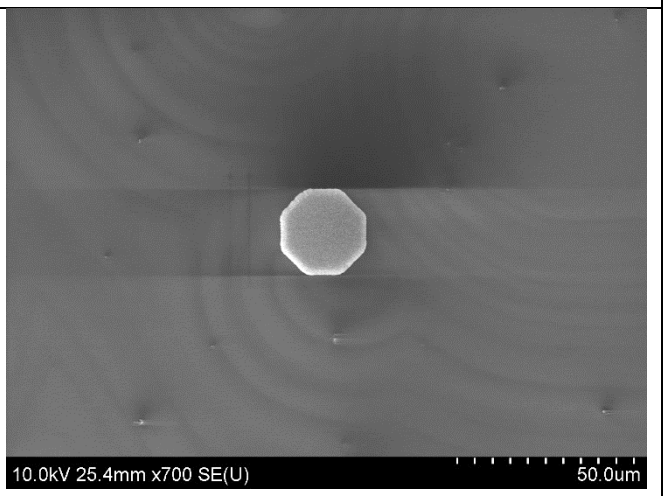

Preparing the Sample for Growth

After sputtering the catalyst, the wafer is covered in photoresist to protect the catalyst surfaces. The wafer is then segmented into pieces using a diamond-tipped scribing tool. To cleave the wafer, the diamond tip is placed on the edge of the wafer and a small cut is etched into the edge of wafer. The wafer is then placed on a glass slide and applied pressure causes the cut to propagate down the wafer. Each piece of wafer cut becomes a sample containing the patterned catalyst.

Before the synthesis of CNTs by CVD, the protective layer of photoresist is removed using consecutive cycles of ultrasonication in acetone followed by isopropyl alcohol (IPA) for about 8 minutes each. After the sample is removed from the IPA, the sample is dried using nitrogen gas.

Synthesis of CNTs

In this study, the synthesis of CNTs took place in a quartz tube with an outer diameter of 25mm, an inner diameter of 20 mm and length of 760 mm using a Thermo Scientific Lindberg Blue M furnace. The gases used were hydrogen (H_2), ethylene (C_2H_4) and helium (He). Figure 3.4 shows the furnace set-up and Table 3.2 lists the steps used. Three "recipes" of various gasses, flow rates and times are used for CNT synthesis. An example of the LabVIEW software interface with a recipe uploaded is shown in Figure 3.5.

The first recipe is the Pre-Baking Recipe. This recipe cleans the quartz tube using dry air and a temperature of 850 ℃ (Step 1). This step eliminates any contaminates remaining from a previous growth. After 50 minutes at 850 ℃ the furnace is opened and the tube is allowed to cool. Once the temperature drops below 200 ℃ the tube is opened and the sample(s) is loaded onto a "boat" (Step 2). The boat is a long piece of silicon wafer that is slightly smaller than the diameter of the quartz tube. The sample and boat are pushed through the tube to a specific position where the growth is best and the tube is sealed. A sampled loaded onto a boat in the quartz tube is shown in Figure 3.6. The outer diameter of the quartz tube is 25 mm while the inner diameter is 20 mm.

The Growth Recipe is next. After the sample is loaded, the tube is flushed for 5 minutes with the three gases H_2, C_2H_4 and He (Step 3). Then only He flows for 5 minutes (Step 4). Next H_2 and He flow for the pre-growth step (Step 5). After 5 minutes of Step 5, a total of 15 minutes into the Growth Recipe, the furnace is closed and the temperature is ramped up to 775 °C. During the growth step (Step 6) the temperature remains at 775 °C and the C_2H_4 that flows over the sample creates the CNTs. The high temperature causes the gases to break down the carbon molecules in the ethylene. The carbon molecules from the C_2H_4 are absorbed into the iron nanoparticles on the catalyst and nucleate CNT growth. The furnace must be opened immediately after the desired growth time has elapsed. The amount of C_2H_4 that flows during this step directly correlates to the growth and height of the CNT pillars. The growth step duration in this study ranged from 25 seconds to 1 minute. To prevent buckling, the pillars were created to have approximately a 1:1 length to diameter ratio where the catalyst diameter, width for rectangles, was the approximate pillar height. The gases are then flushed out of the tube with He for 20 minutes (Step 8).

The final recipe is the Finishing Recipe and is used to clear the quartz tube and pipe lines of gases and the tanks are closed (Steps 9 and 10). The tube is opened and the sample is removed using a smaller metal rod that extends past and underneath the boat to pull it towards the opening.

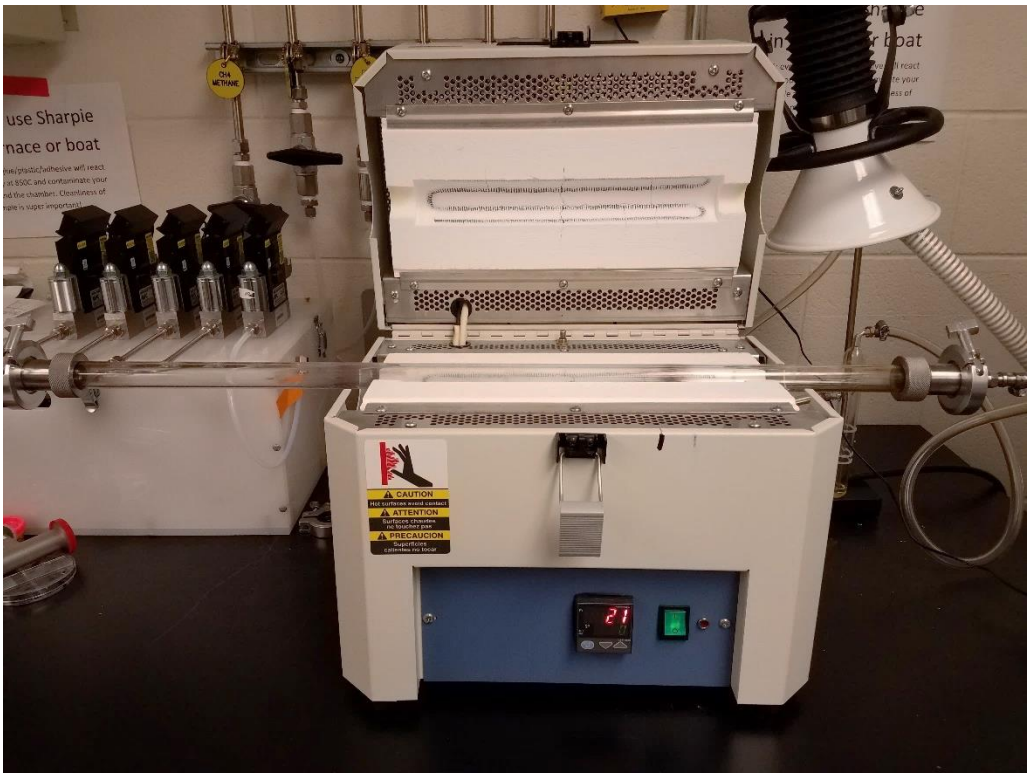

Figure 3.4 Tube furnace set-up for CNT growth.

Table 3.2 Recipes and steps for CNT growth.

Step	**Description**	**Gases**	**Temperature**	**Time**
1.	Begin Pre-Baking Recipe	Dry Air – 1.5 sccm	Ramp up to 850 °C *open furnace at 50 minutes into step, set furnace to room temperature	75 minutes
2.	End Pre-Baking Recipe Load Sample	–	< 200 °C	–
3.	Begin Growth Recipe	H_2 – 500 sccm C_2H_4 – 500 sccm He – 5000 sccm	< 200 °C	5 minutes
4.	Flush Tube	He – 1000 sccm	< 200 °C	5 minutes

Table 3.2 (cont.)

5.	Pre-Growth	H_2 – 100 sccm He – 400 sccm	< 200 °C *ramp up to 775 °C after 5 minutes	25 minutes
6	CNT Growth	H_2 – 100 sccm C_2H_4 – 100sccm He – 400 sccm	775 °C *furnace opened immediately after growth is complete, set furnace to room temperature	< 1 minutes
7	Flush Tube	He – 1000 sccm	< 775 °C	5 minutes
8	Flush Tube End Growth Recipe	He – 100 sccm	< 775 °C	20 minutes
9	Finishing Step Recipe	H_2 – 300 sccm C_2H_4 – 50sccm He – 400 sccm	< 775 °C	5 minutes
10	End Finishing Recipe Remove Sample	–	< 200 °C	–

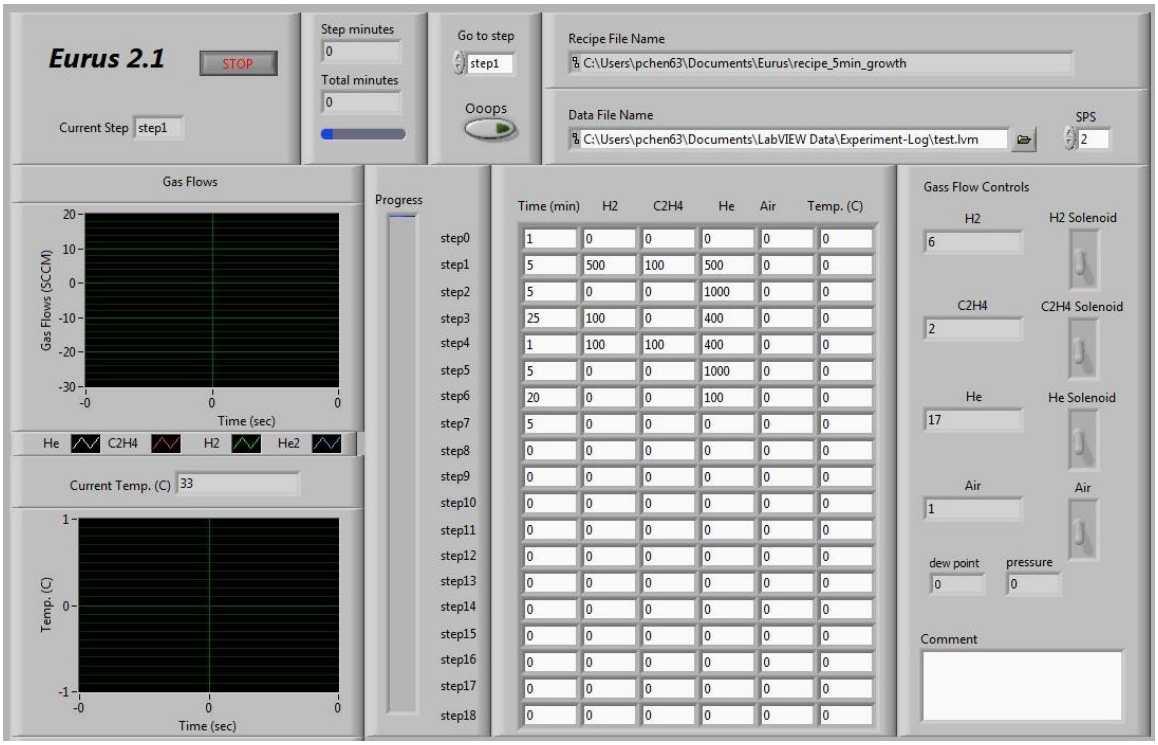

Figure 3.5 The LabVIEW interface with the Growth Recipe populated. Note that the steps listed correspond to the Growth Recipe listed in Table 3.2.

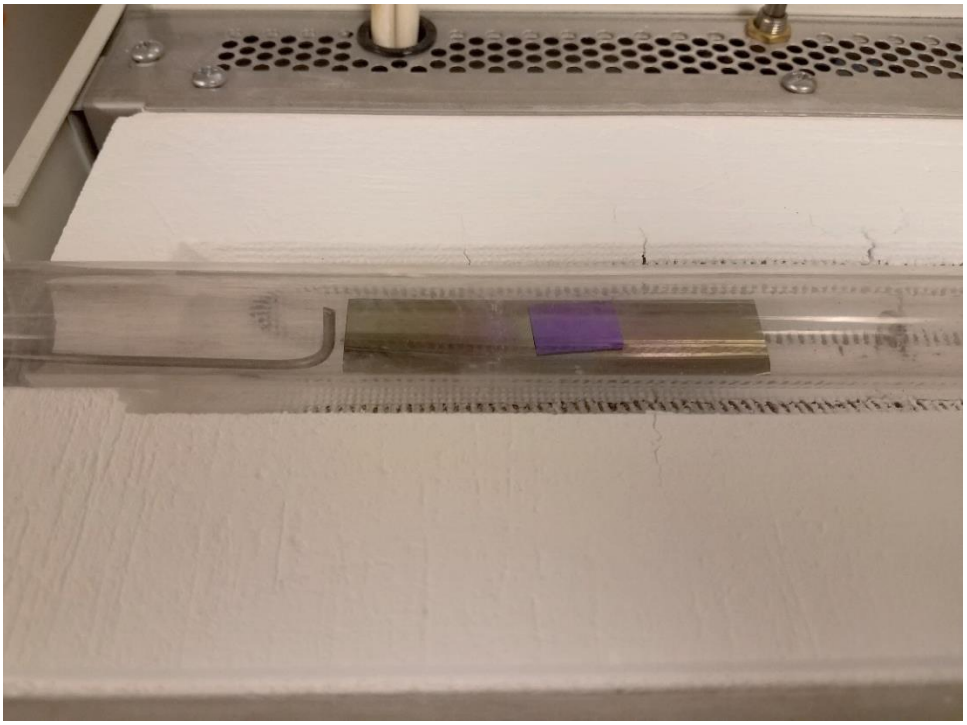

Figure 3.6 The silicon sample and boat are inserted and removed from the quartz tube using a metal rod.

3.3. High Temperature Ceramic Coatings

Two high temperature ceramic coatings were used in this study. Hafnium diboride (HfB_2) and the polymer derived silicon oxycarbide (SiOC).

3.3.1. Hafnium Diboride Coating

The HfB_2 coating method was performed by Tushar Talukdar of Professor John Abelson's research group in Materials Science and Engineering at the University of Illinois. The CVD set-up included a 1" diameter Pyrex tube closed on end with a glass-metal adapter on the other end. A hafnium diboride precursor of $Hf[BH_4]_4$ was used. The growth procedure is described in Table 3.3 and Figure 3.7 depicts how the HfB_2 coating affects the sample.

Table 3.3 Growth recipe for HfB_2 coating.

Step	Description
1	Load sample into tube and chamber.
2	Set base pressure in the chamber ~ 10^-7 Torr.
2	Bake sample at 350 ℃ for 30 min to remove moisture from sample and tube surface. Ramp rate for baking: 20 ℃/min.
4	After bake, cool down to room temperature.
5	Close gate valve between tube and turbo pump for the process to be non-flow/static during growth.
6	Load required $Hf[BH_4]_4$ precursor – set pressure for precursor.
7	Ramp rate slow: 1 ℃/min.
8	Hold at 200 ℃ for 2 hours.
9	Cool down to room temperature.
10	Remove sample.

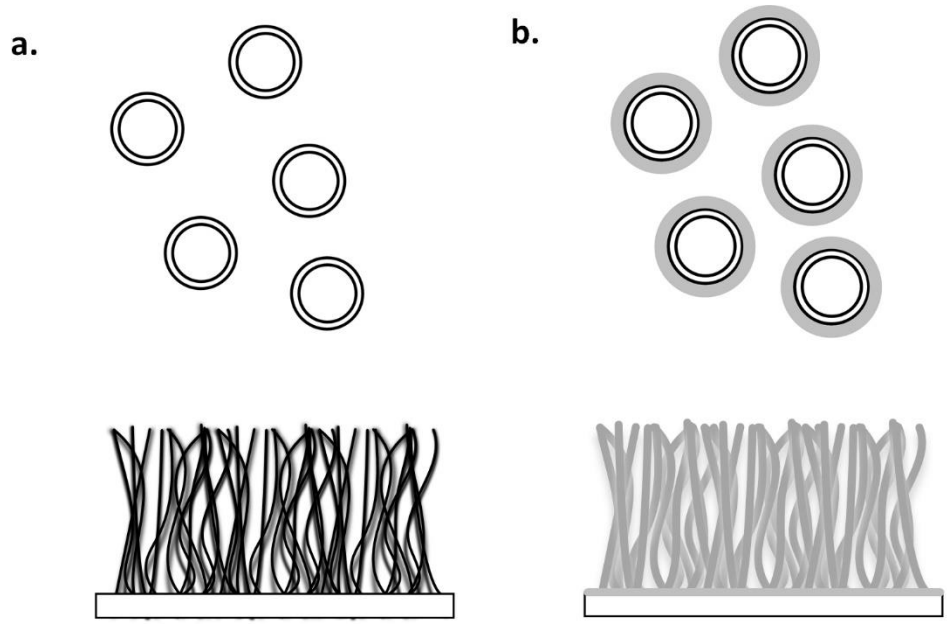

Figure 3.7 a.) A sample of uncoated CNTs depicting the outer and inner CNT diameters. b.) Coating accumulates on the outer diameter of the CNTs within the sample.

A range of thicknesses was desired to test how coating thickness affects mechanical behavior. Table 3.4 lists the thicknesses from uncoated samples to fully coalesced coated samples. It was found that the amount of CNTs in the sample greatly affects the amount of thicknesses. This is because in larger sized CNT forests there is more surface area for the precursor to coat.

Table 3.4 Coating thickness for HfB_2 coated pillars.

Average Coating Thickness	**SEM Image** *note: varying scales
Uncoated = 0 nm	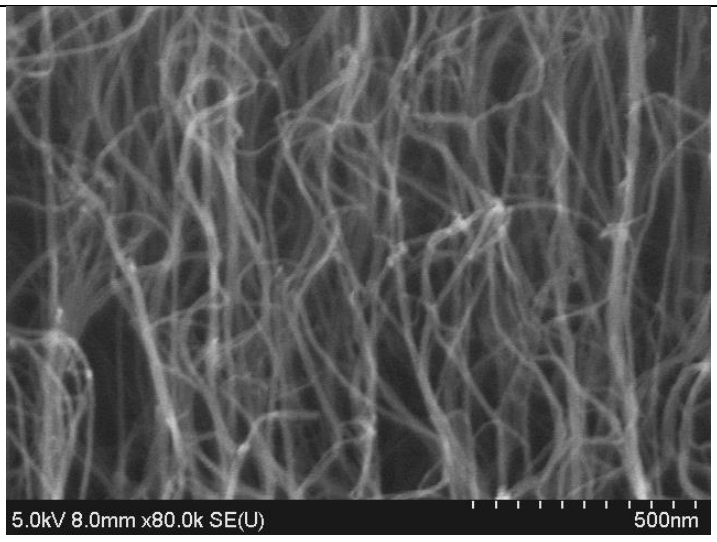

Table 3.4 (cont.)

Coating ≈ 3 nm	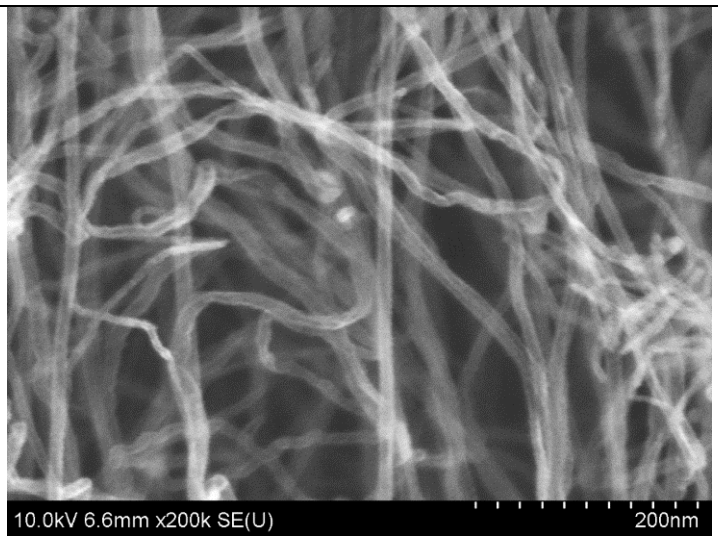
Coating ≈ 7 nm	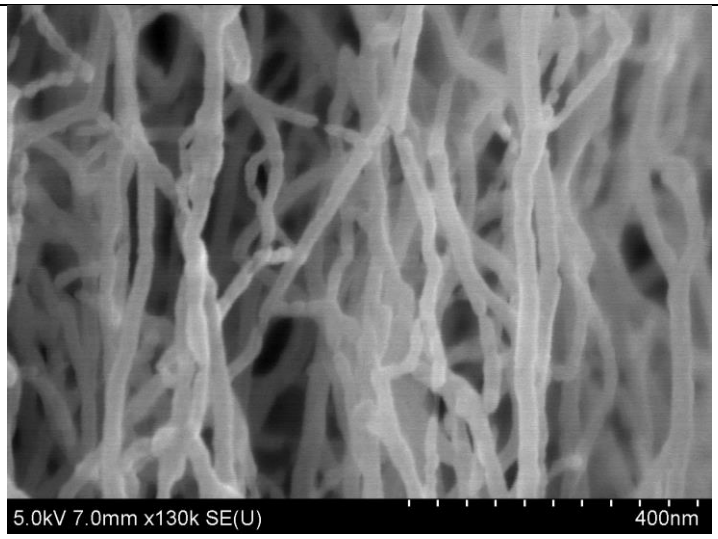
Coating ≈ 12 nm	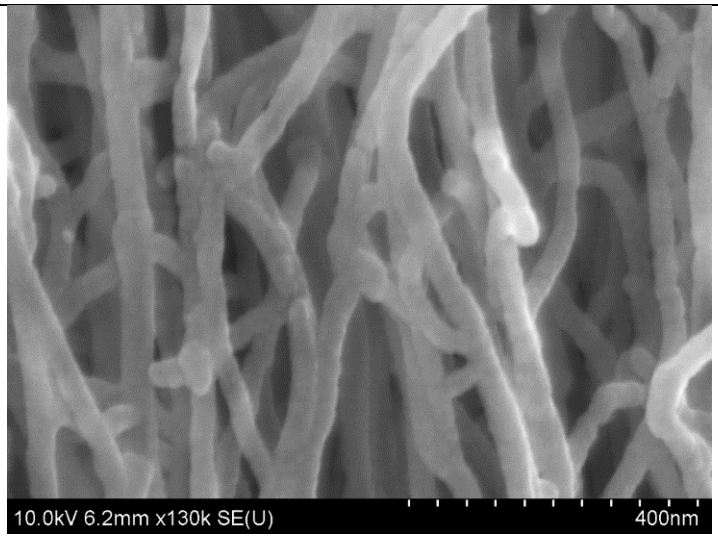

Table 3.4 (cont.)

Coating ≈ 17 nm	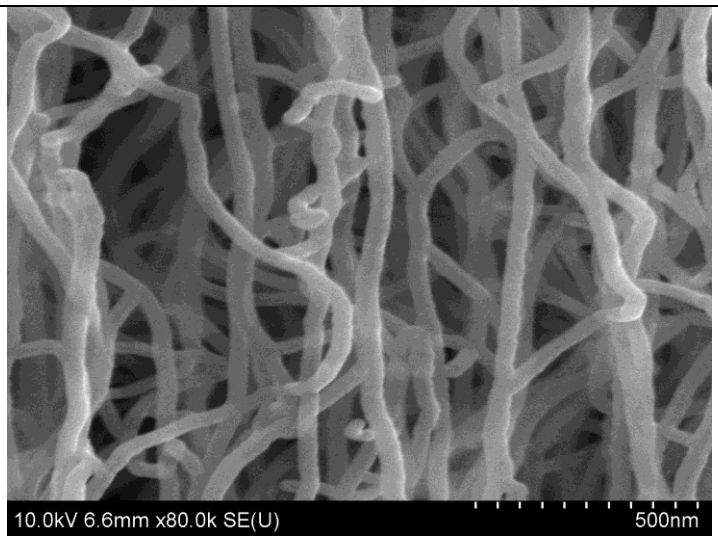
Coating ≈ 28 nm	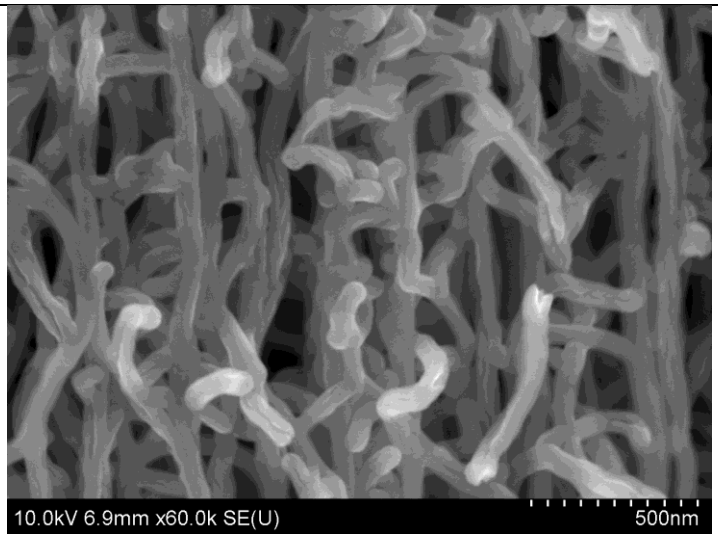
Coating ≈ 50 nm	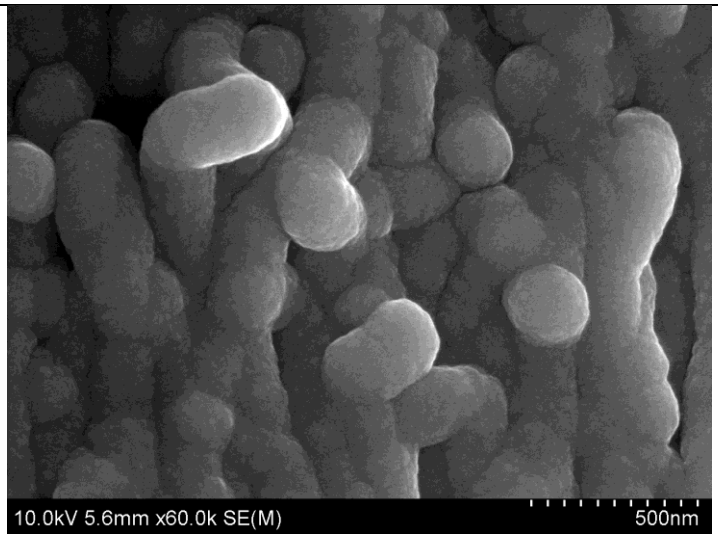

Table 3.4 (cont.)

Coating – coalesced *not tested	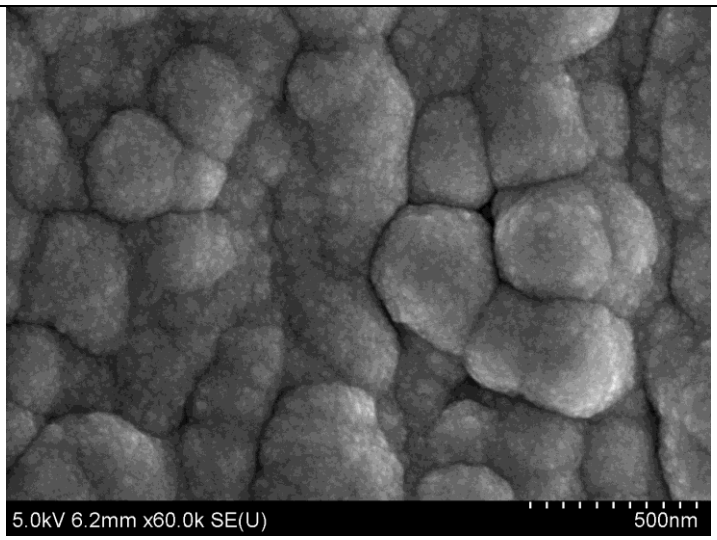

3.3.2. Polymer Derived Ceramic Coating

Recent studies [10], [18] show that polymer derived ceramics (PDCs) can be used to infiltrate porous materials. The coating process for PDC was spin-coating. A solution was created from a 14:1 ratio of (mercaptopropyl) methylsiloxane – dimethylsiloxane copolymer and vinylmethoxysiloxane homopolymer based on Eckel et al. study [10]. The materials were ordered from Gelest Inc. The polymers were pipetted into an amber bottle and mixed on a stir plate using a stir bar.

The sample was spin-coated using a SCS G3P spin-coat machine as shown in Figure 3.8 a.) A sample is loaded into the SCS G3P spin-coat machine. b.) A close-up of the sample on the vacuum stage.. A pipet was used to drop 2-3 drops of the solution onto the wafer sample and the sample was spun using the speeds provided in Table 3.5. The sample was then subjected to a slow heating cycle of pyrolysis in a tube furnace. Pyrolysis cures the polymer solution into a PDC of Si-OC coated CNTs. These steps are listed in Table 3.6.

Table 3.5 PDC spin-coat steps.

Step	Description	Speed	Time
1	Load sample into spinner	-	-
2	Dry run of sample *Check orientation	1000 rpm	15 seconds
3	Add 2-3 drops of PDC solution	-	-
4	Low spin speed	400 rpm	15 seconds
5	High spin speed	1500 rpm	45 seconds

Table 3.6 PDC pyrolysis steps.

Step	Description	Gases	Temperature	Time
1	Begin Pre-Baking Recipe	Dry Air – 1.5 sccm	Ramp up to 850℃ *open furnace at 50 minutes into step, set furnace to room temperature	75 minutes
2	End Pre-Baking Recipe Load Sample	-	< 200℃	-
3	Begin Annealing Cycle	He – 500 sccm	Ramp up to 1000℃ at a rate of 1℃/min	~1000 minutes
4	Annealing – Hold	He – 500 sccm	Hold	60 minutes
5	Annealing – Ramp Down	He – 500 sccm	Ramp down to room temperature at a rate of 3℃/min	334 minutes
6	End Annealing Cycle Remove Sample	-	< 200℃	-

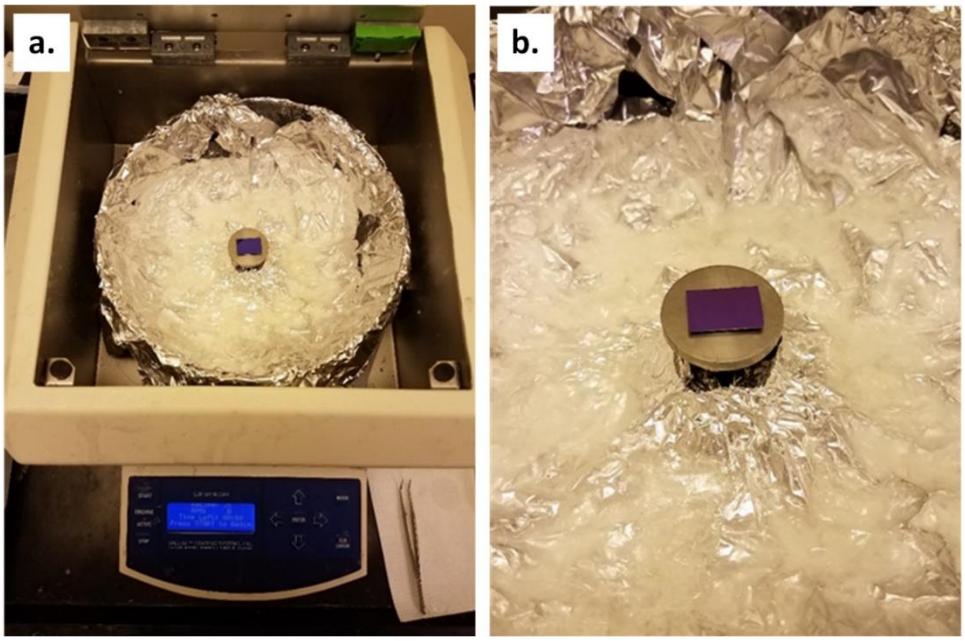

Figure 3.8 a.) A sample is loaded into the SCS G3P spin-coat machine. b.) A close-up of the sample on the vacuum stage.

3.4. Nanoindenter Instrument

Traditional indentation is used for hardness testing. Rockwell hardness testing is example of a test used to determine a material's hardness. The conical diamond round tip is pressed into the material and leaves behind a cavity. The cavity is then measured. However, many studies have used a diamond flat-punch in place of the Berkovich or a round tip. This flat-punch can be used to compress the pillars having a smaller diameter than the tip, and in this case the pillars' area is the contact area.

Testing Apparatus

The micropillars in this study were tested using a Hysitron TI 950 TriboIndenter nanoindenter. The nanoindenter is an automated instrument that uses feedback-control to perform nanomechanical testing. Hysitron software called TriboScan™ Professional was used to set-up the load function and perform testing. The instruments operate using a load cell that determines the maximum load capacity. The two-dimensional standard transducer load capacity was predicted to be too low for the thicker coated micropillars. The high-load transducer was used instead. It has a maximum normal force of 10 N and an 80 µm maximum displacement. The diamond flat-punch was ordered from Micro Star Technologies Inc. The tip was fitted to fit the high-load transducer. It has a 150 µm and the dimensions can be seen in Figure 3.10 and Figure 3.11. The nanoindenter used in this study is located at the Materials Research Laboratory at the University of Illinois at Urbana-Champaign.

Table 3.7 Nanoindentation testing information.

Instrument	Hysitron TI 950 TriboIndenter
Program	TriboScan™ Professional
Load Cell	Hysitron 3D OminProbe
Vacuum Stage Dimensions	12 mm diameter circles
Tip Dimensions	150 µm diameter flat punch

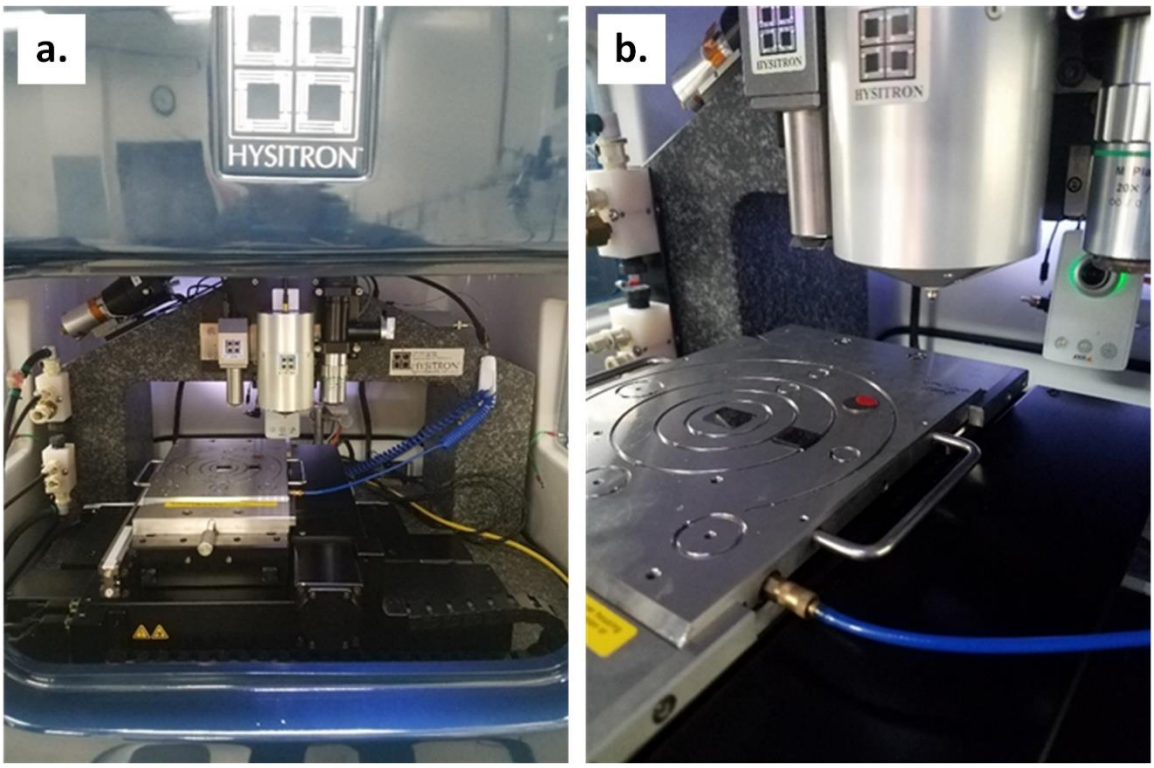

Figure 3.9 a.) The Hysitron nanoindentation instrument. b.) Vacuum stage with two rectangle silicon samples and a calibration sample of red wax.

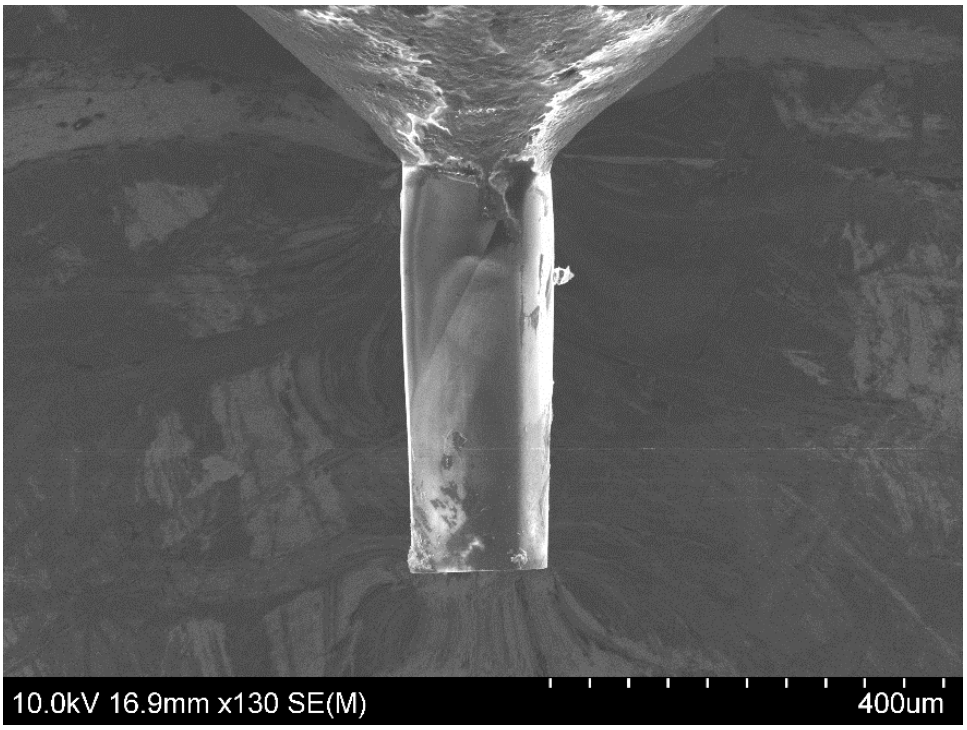

Figure 3.10 Side view of the diamond flat-punch nanoindentation tip.

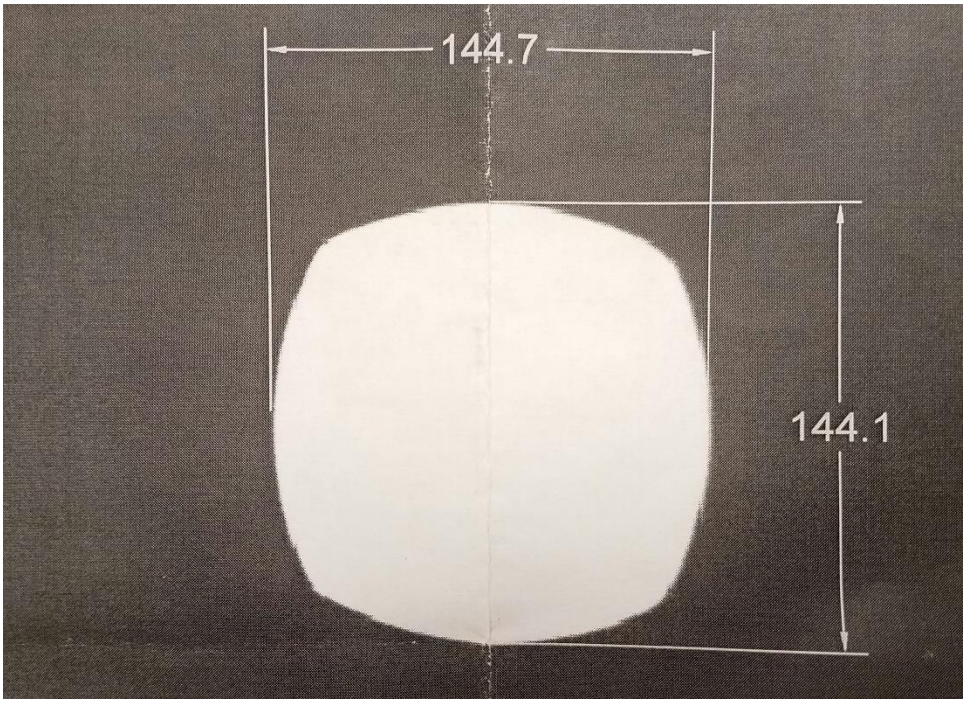

Figure 3.11 The dimensions of the flat-punch tip.

3.5. Nanoindentation Testing

Each nanoindentation testing session began with installing the appropriate transducer and stage. The flat-punch tip was screwed onto the high-load transducer and the transducer was mounted into the instrument. A vacuum stage with 12 mm circles and magnetic areas was used to hold down the samples. After the Hysitron software is opened and correct transducer selected, the instrument performs equipment checks and homes the transducer.

Calibration

Next is a series of calibrations. Each transducer has its own calibration file that needs to be updated before every testing session. The transducer and tip are calibrated together and the measured values are recorded in the software. These values change with each use and vary from tip to tip. It is important that the user ensures the values fall within the appropriate range for that transducer before continuing.

Next is a calibration air indentation. The air indentation is performed in the "air." The air indent data ensures that the tip and transducer are performing properly. After this data is taken the user checks that the values fall within the appropriate range before continuing.

The final calibration is the stage-to-tip calibration. A calibration sample is prepared by dropping melted wax onto a magnetic disc. The magnetic disc is then placed on the stage. A sample boundary is created for the wax sample, described later. A load of 8000 μN was used to calibrate the flat-punch tip. The wax allows the user to visibly see the tip's indentation. The software provides the means to center the tip over of this indentation. An example of the wax disc on the stage is shown in Figure 3.9 and an example of the wax indentation in the software is shown in Appendix A.

Sample Boundaries

After calibration is completed, sample boundaries must be mapped out. Every sample to be tested needs a sample boundary. The sample boundary is a set area that is generated by the software and only allows the instrument to test within that area. If the sample area extends beyond the software's boundary limits, a new sample boundary needs to be created. The number of pillars that can fit within a sample boundary depends on the pillar size and spacing. Once a sample boundary is created, the instrument will use a technique called 'Quick Approach' to determine the height of the sample area. The instrument stores this height from the tip in its homed position to the sample surface and uses this distance for the entire sample within the sample boundary. When a new sample boundary is created, the tip to sample distance needs to be re-recorded.

Sample Focus

During testing, the user manually uses the software to view the sample and center the tip over the location of testing. Then the optics in the z-direction are moved down until the sample is in focus. The focus for these samples was on the top of the pillars. An example of a pillar centered under the optics is shown in Appendix B.

Load Function

The load function determines how and to what load the pillars are tested. The software supplies standard load functions, but the user can change the inputs to adjust various parameters such as loading time, the number of segments and the data acquisition rate. Figure 3.12 shows an example of a load function displayed in the TriboScan software. The software also has the capability for displacement control or load control. It was determined that a load-controlled function improved the data collection for uncoated and thinly coated pillars because of the collapsing behavior. All data provided in the results was from a load-controlled load function ranging from a 0.1 mN to 1100 mN peak load applied to the pillars.

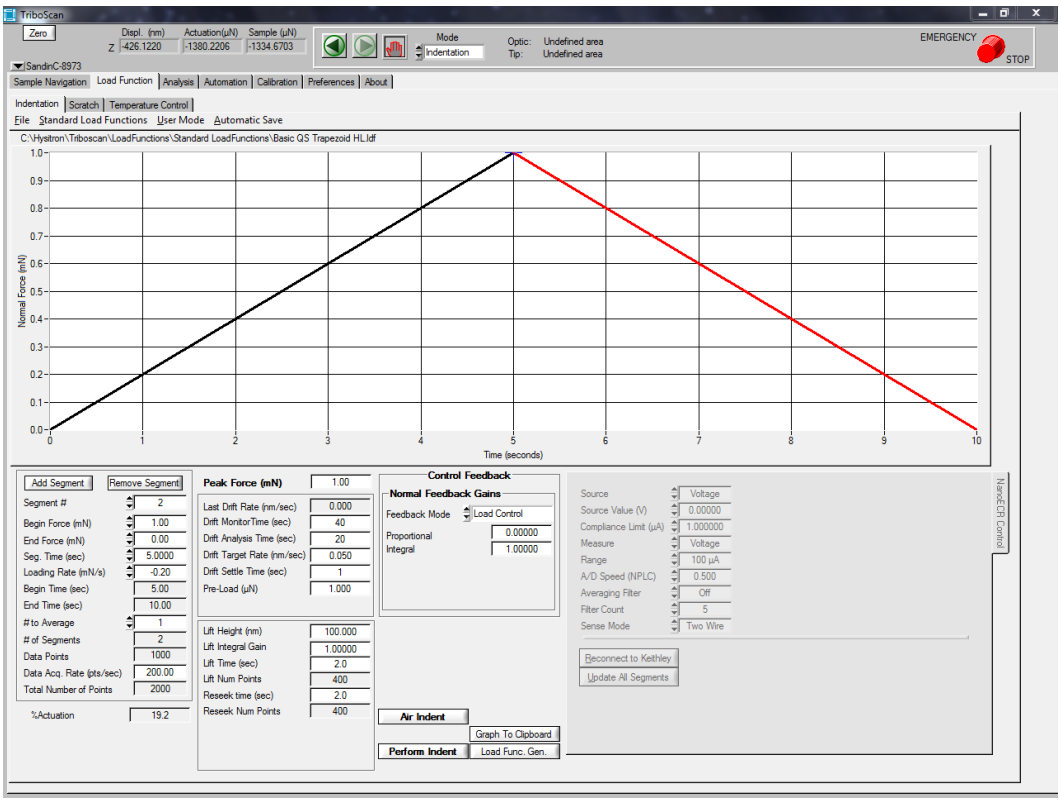

Figure 3.12 An example of a load function in the TriboScan software.

CHAPTER 4: RESULTS

4.1. Introduction

This chapter provides the results of the nanoindentation testing described in the previous chapter. The data is presented as stress-strain plots for uncoated carbon nanotube (CNT) pillars, hafnium diboride (HfB_2) coated pillars and polymer derived ceramic pillars. The data for each thickness is divided into two plots. The first plots show the data of the tested pillars before they reached failure. For each coating condition, a stress value is reported in the legend which corresponds to the load entered in the indenter program to test the pillars without inducing failure. The second plots show the data of pillars that failed during testing when the programmed load is increased beyond the elastic region of the pillar. The pillar failure was determined using scanning electron microscope (SEM) images. A description of the plots and the observations of the failure modes will be discussed briefly in this chapter and more in depth in Chapter 5.

4.2. Stress-Strain Plots for Uncoated Pillars

A flat-punch diamond tip (Figure 3.10) was used to test all pillars. The tip was manufactured by Micro Star Tech. The tip compatibility was selected for the high-load head transducer of nanoindenter. It was determined that uncoated CNT pillars could only be accurately tested at low loads due to the collapsing behavior.

Stress up to 0.16 MPa can be programmed in the indenter program showing a quasi-elastic behavior (Figure 4.1 a.). The quasi-elastic behavior is not necessarily linear during loading. The pillars do not fully recover their original length during unloading, which is shown by the hysteresis loop between loading and unloading. It is still called here quasi-elastic because the pillars do not collapse or buckle up to this stress. As the stress approaches 0.2 MPa (Figure 4.1 b.), a qualitative change in the loading stress-strain response is observed where a plateau region forms in the data. SEM images show that the uncoated CNT pillars begin collapsing. This collapsing behavior was also observed in thinner HfB_2 coated pillars as well. The collective buckling folds evident in Figure 4.2 c-d. are also seen in other studies [6], [13], [16].

A problem mentioned by Poelma [6] was adhesion to the tip for uncoated pillars with small diameters. This was an issue for the Rectangle pillars tested in this study (Figure 4.2 b.). This data was not included in the results. A thin layer of gold was sputter-coated over the uncoated pillars before testing. Double-sided tape was used to remove the pillar that adhered to the tip by using the ‘Quick Approach’ feature to lightly touch the pillar on the tip to the tape.

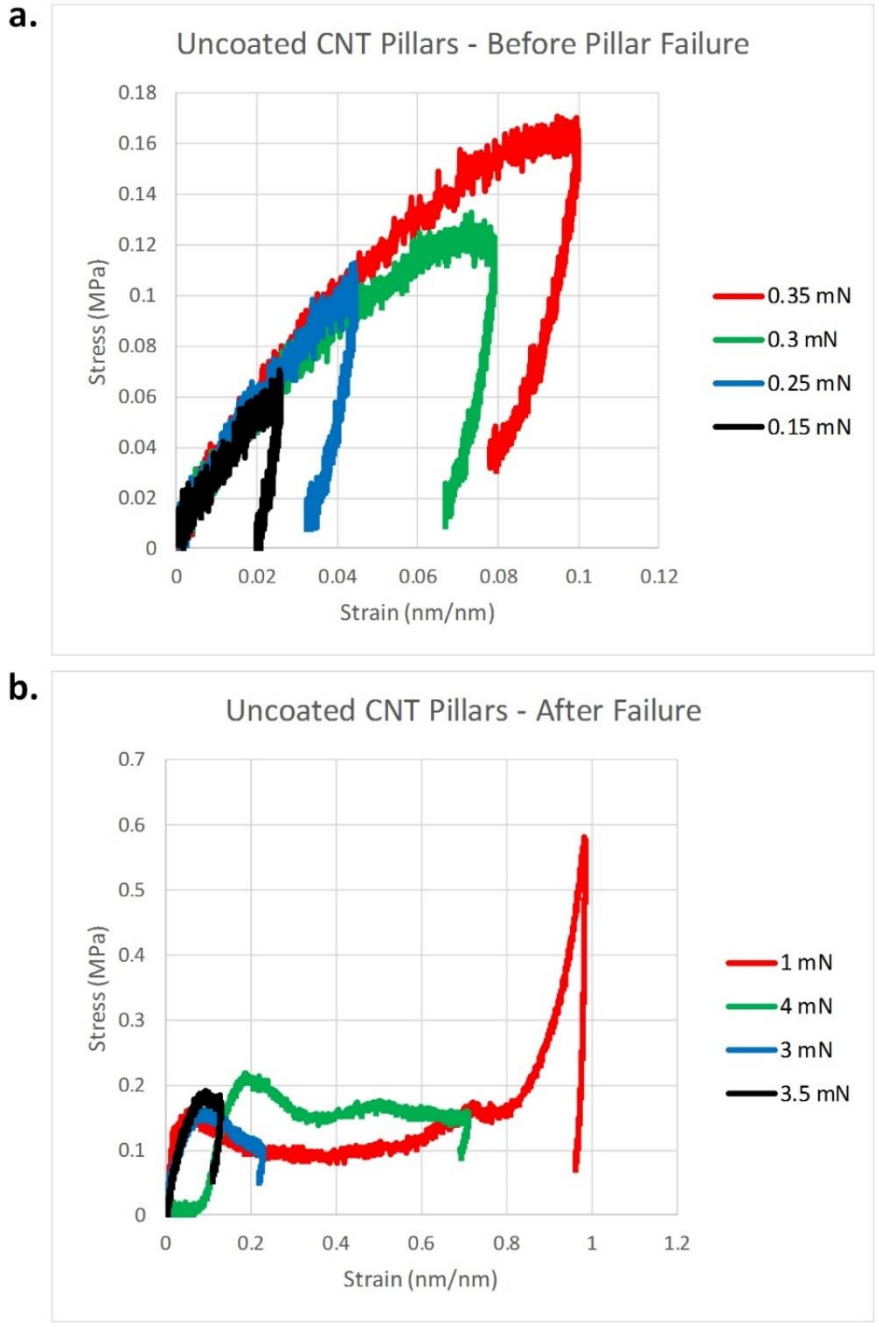

Figure 4.1 Stress-strain curves for the uncoated CNT pillars. a.) Data before pillar failure. b.) Data after pillar failure by collapse.

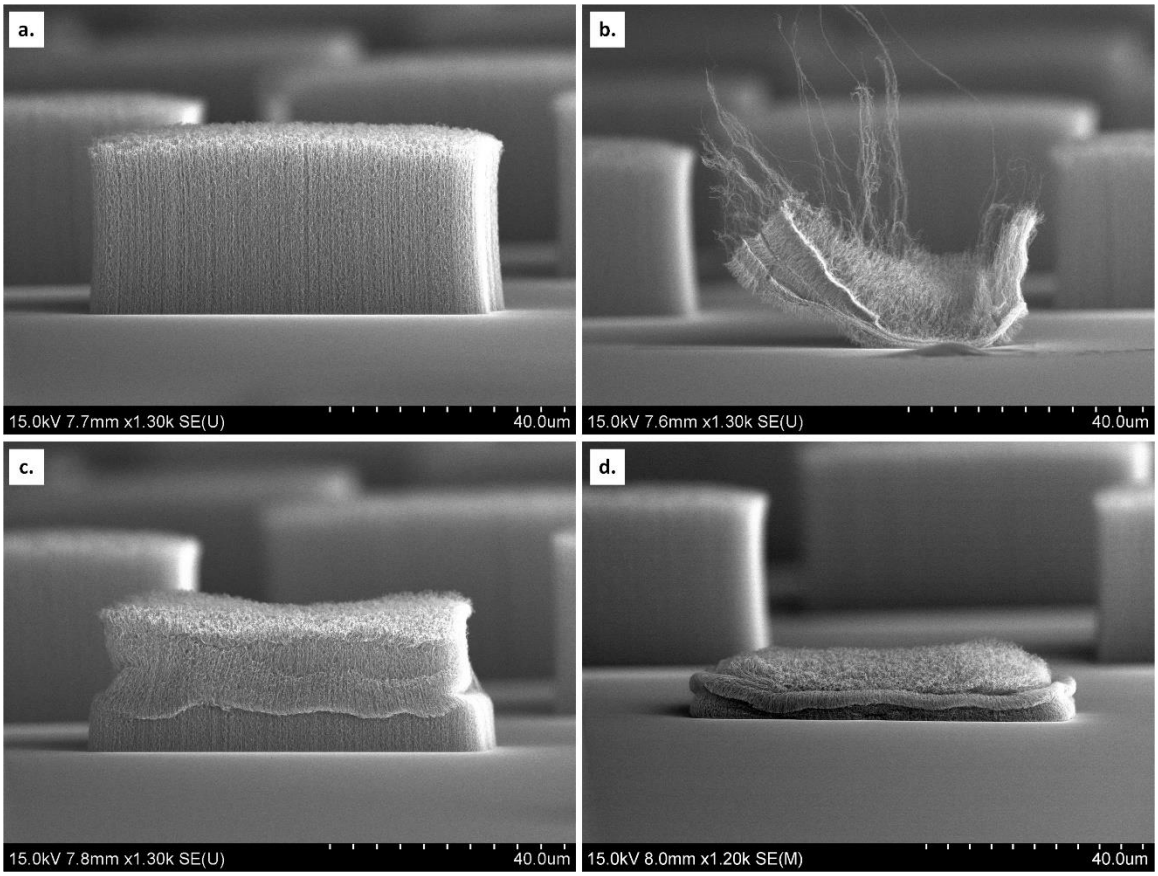

Figure 4.2 Tested uncoated pillar SEM images. a.) Tested pillar before failure. b.) Pillar adhesion to tip. c.) Pillar failure by buckling. d.) Pillar failure by collapse with buckling folds.

4.3. Stress-Strain Plots for HfB_2 Coated Pillars

3 nm HfB_2 Coating Thickness

The goal for the HfB_2 coated pillars was to test a range of thicknesses and observe how the mechanical behavior changes. The stress-strain curves of the 3 nm HfB_2 coated pillars in Figure 4.3 a. show similar stress values before failure as the uncoated pillars, up to 0.18 MPa. The shape of the loading curve for low stresses is more linear compared to the uncoated samples. The maximum stress value for the collapsed pillars is about 0.3 MPa compared to the uncoated pillars stress value of 0.2 MPa.

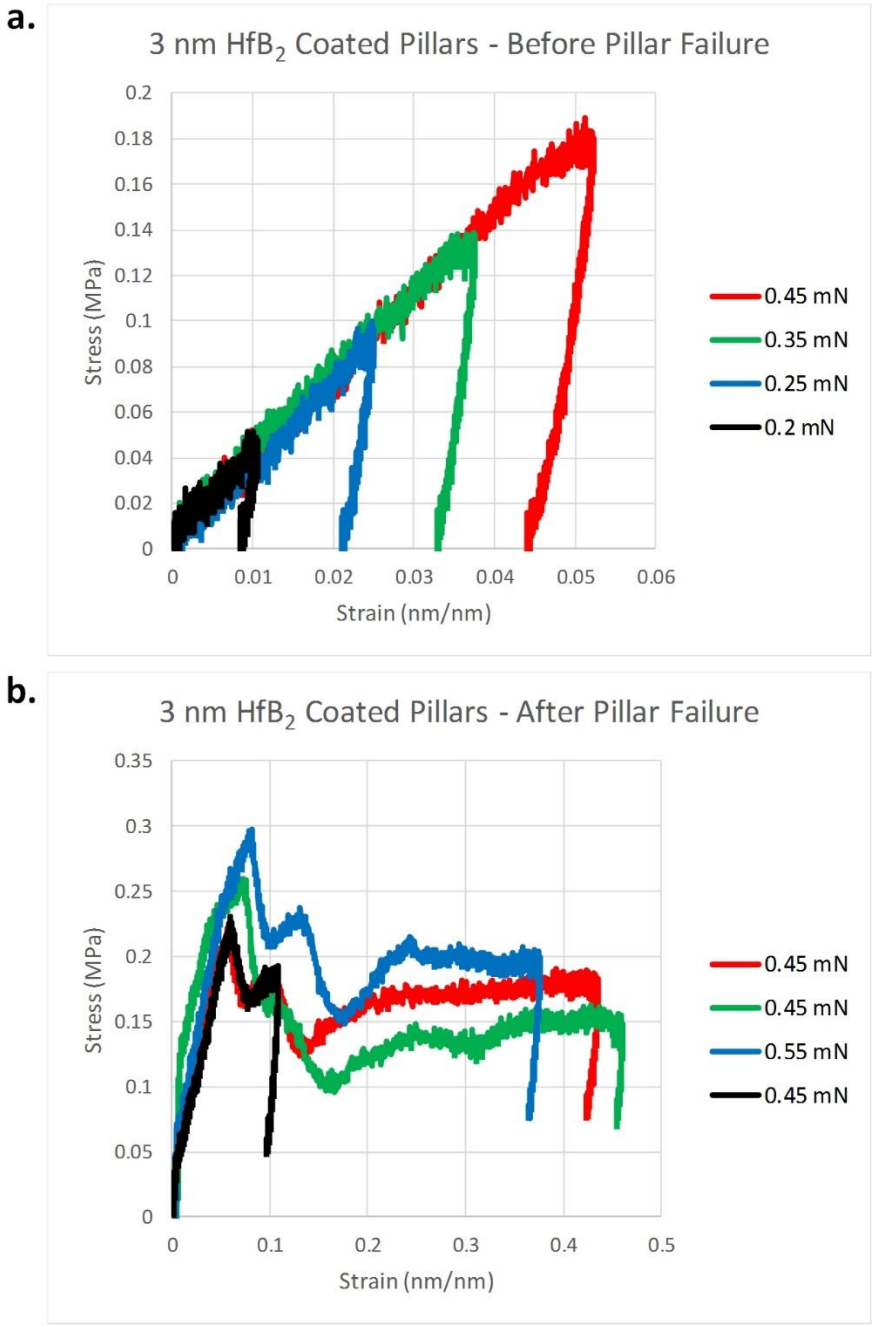

Figure 4.3 Stress-strain curves for the 3 nm HfB_2 coated CNT pillars a.) Data before pillar failure. b.) Data after pillar failure by collapse.

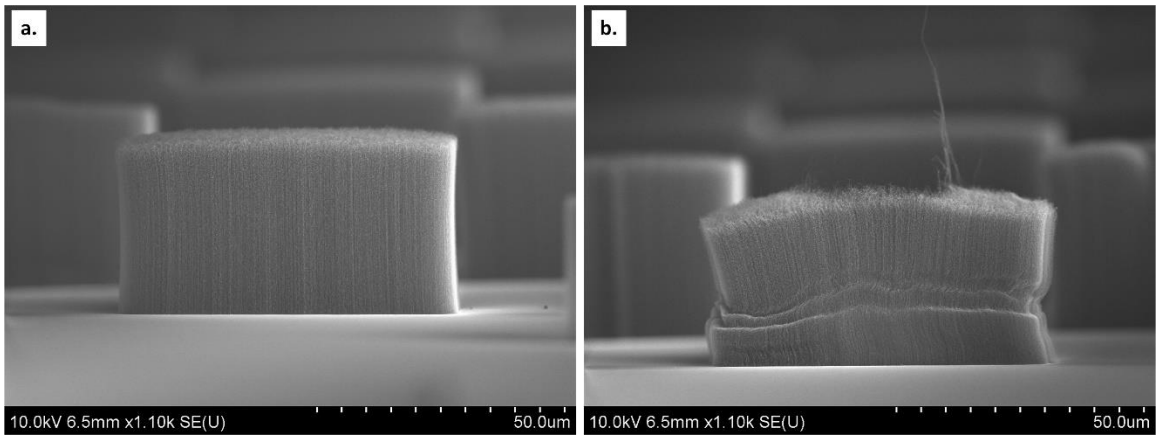

Figure 4.4. Tested 3 nm HfB_2 coated CNT pillars. a.) Before pillar failure. b.) After pillar failure with buckling folds and adhesion to tip.

7 nm HfB_2 Coating Thickness

The 7 nm HfB_2 coated pillars reached 0.25 MPa (Figure 4.5 a.) stress before pillar failure. The loading curves start with a large slope, then the slope decreases but remains linear until reaching the maximum stress value of about 0.5 MPa.

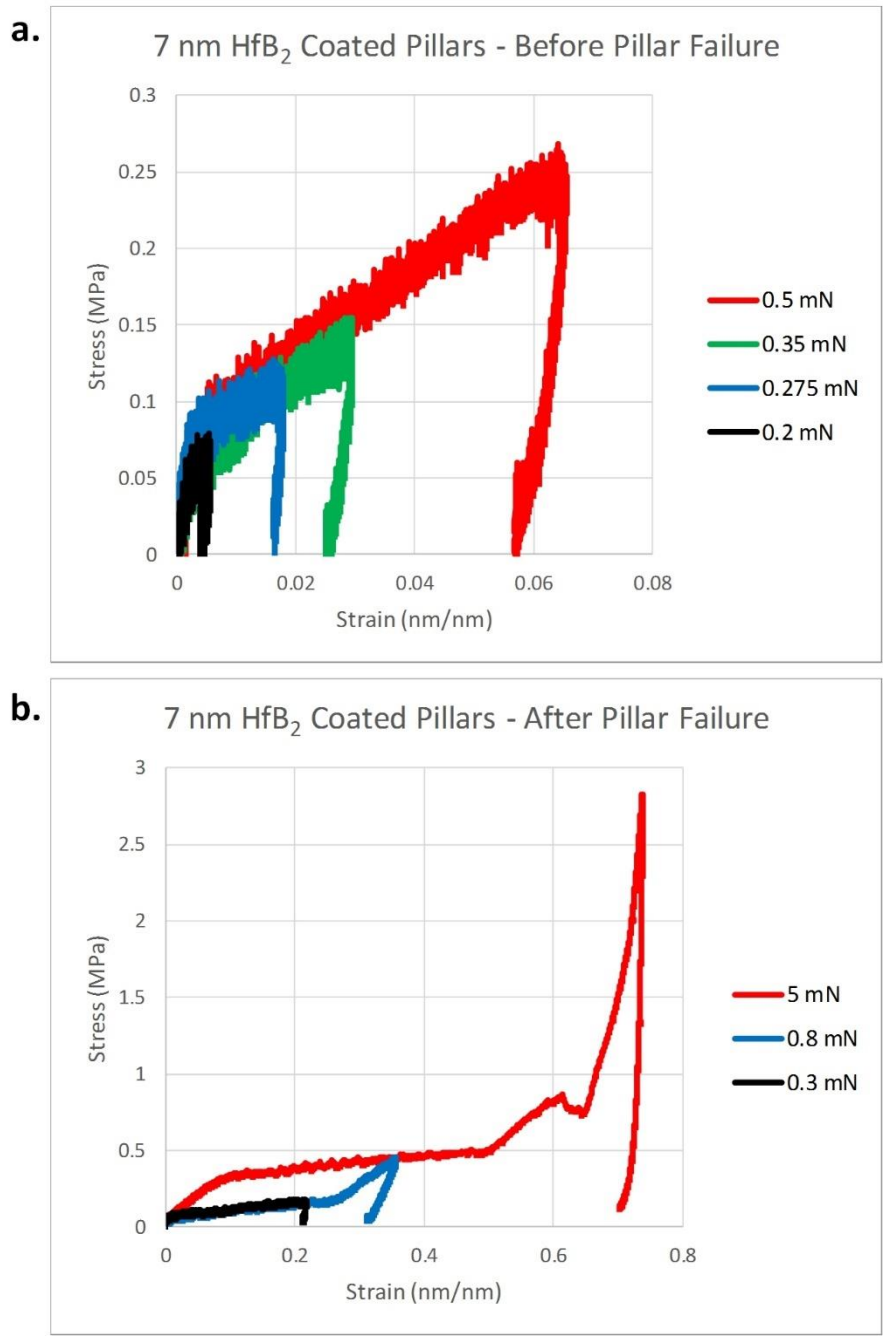

Figure 4.5 Stress-strain curves for the 7 nm HfB_2 coated CNT pillars a.) Data before pillar failure. b.) Data after pillar failure by fracture.

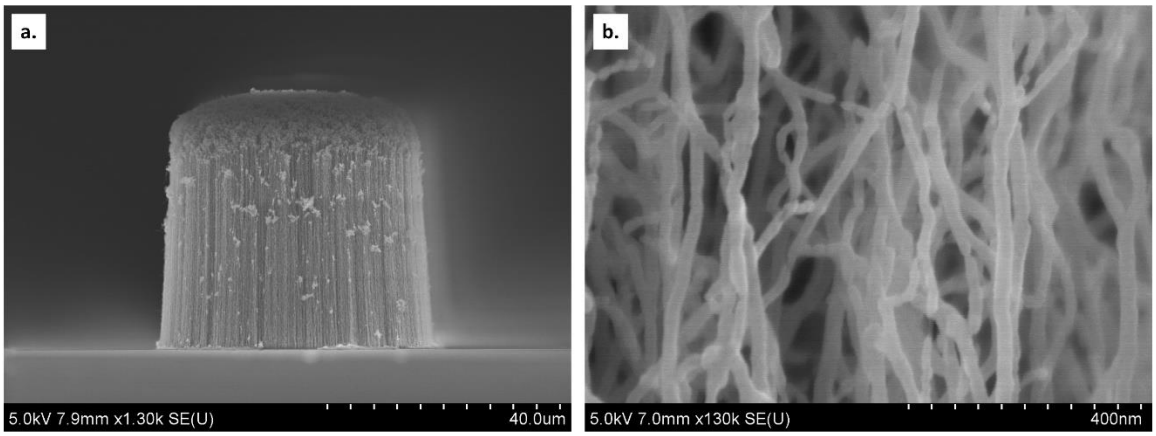

Figure 4.6 a.) Untested 7 nm HfB_2 coated CNT pillar. b.) 7 nm HfB_2 coated CNTs.

12 nm HfB_2 Coating Thickness

For the 12 nm HfB_2 coating there is a significant increase in stress. The stress values before failure reach 5 MPa compared to under 1 MPa for 0, 2, and 7 nm. The loading curve is also linear, and there is significant hysteresis during unloading. The maximum stress for failed pillars is an average of 7 MPa and it was also under 1 MPa for the 0 nm, 2 nm and 7 nm coatings. Figure 4.8 c-d. shows that the coating is not always conformal. Gaps in the coating or bare CNTs can be seen. This could be a result of CNT fiber pull-out or cracking in the coating due to residual stresses. Kessman et al. [20] notes that pull-out may be caused by residual stresses from shrinkage.

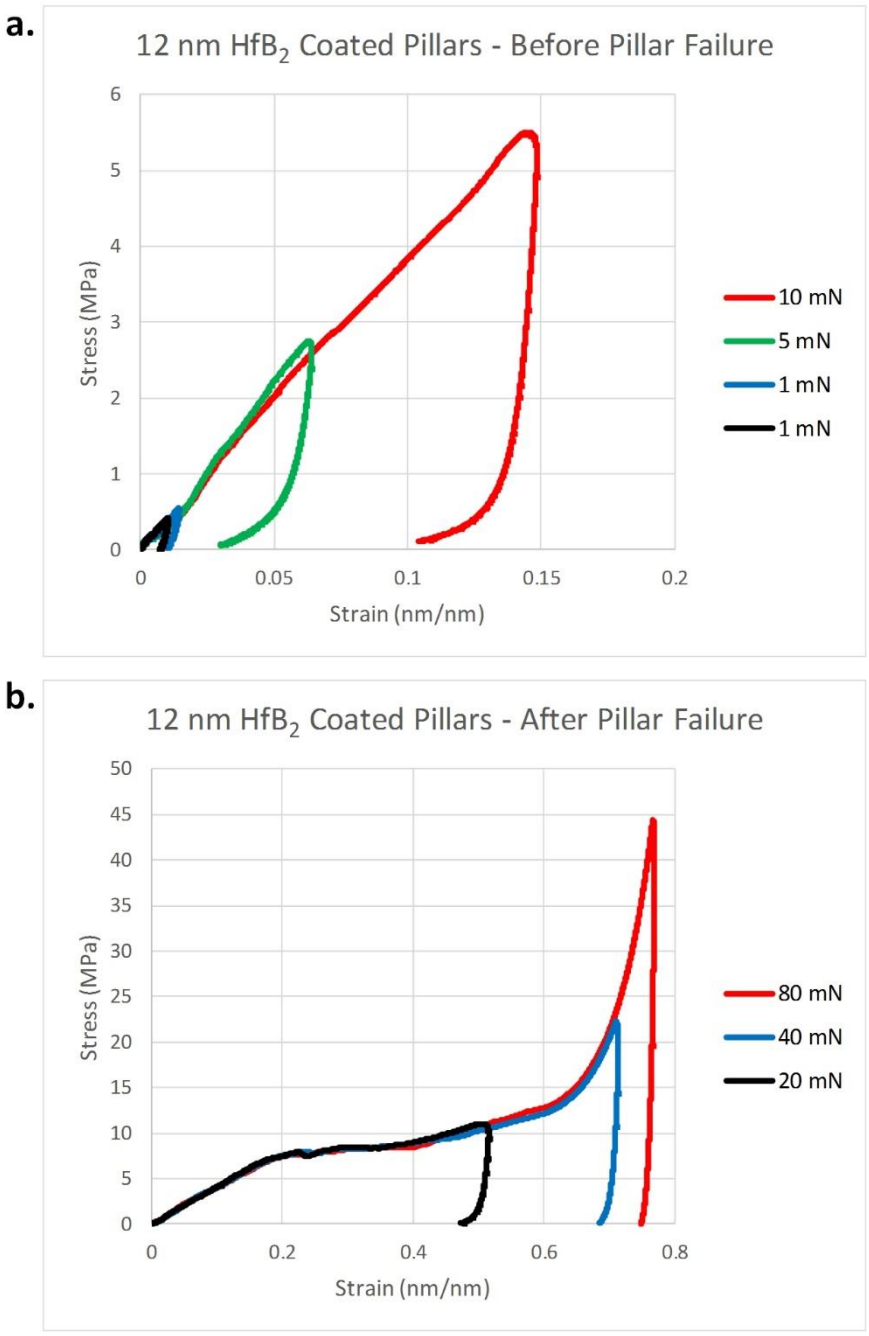

Figure 4.7 Stress-strain curves for the 12 nm HfB_2 coated CNT pillars a.) Data before pillar failure. b.) Data after pillar failure by collapse and fracture.

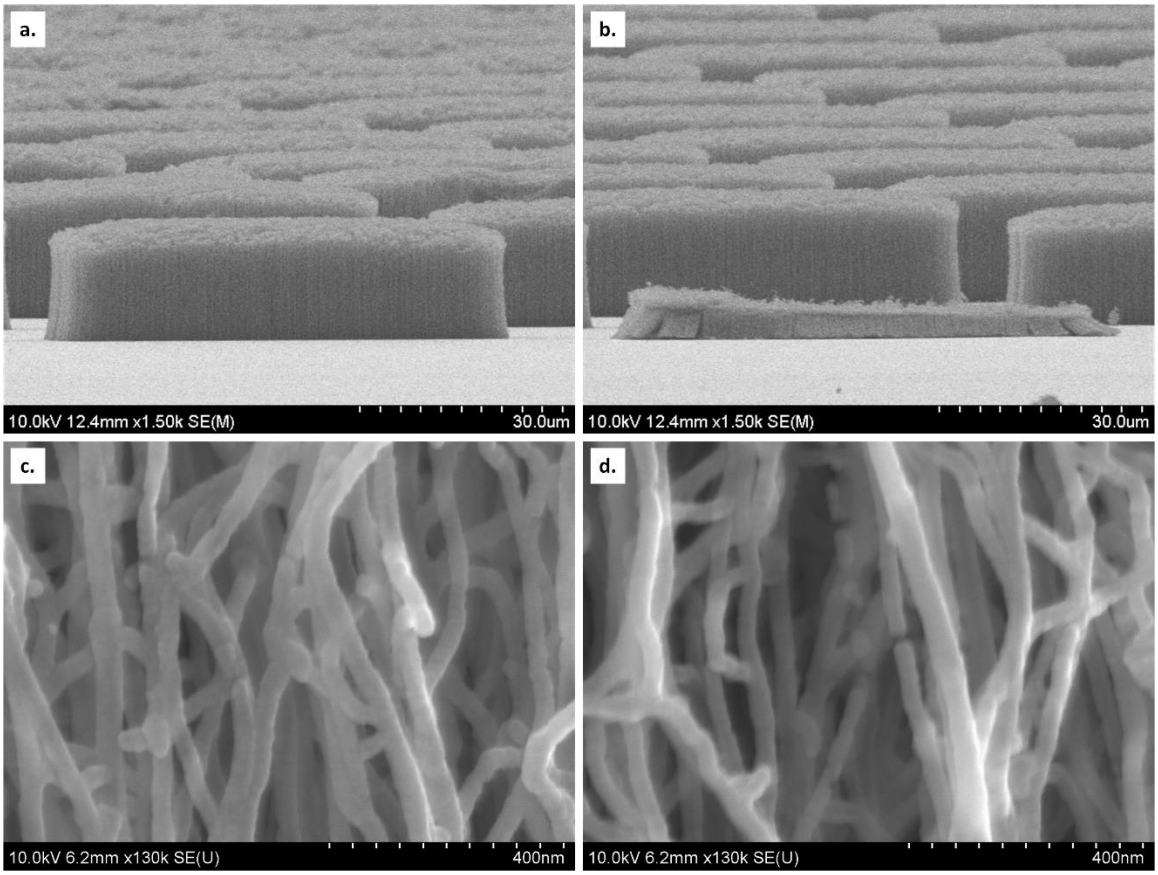

Figure 4.8 Tested 12 nm HfB2 coated CNT pillars. a.) Tested pillar before failure. b.) Pillar failure by collapse and fracture. c-d.) Coated CNTs showing gaps of bare CNTs in coating.

17 nm HfB_2 Coating Thickness

The 17 nm HfB_2 coating shows similar trend to the 12 nm coating. Figure 4.9 show the stress values before failure are close to 5 MPa and the maximum stress value for the failed pillars is slightly higher than the 12 nm at 10 MPa.

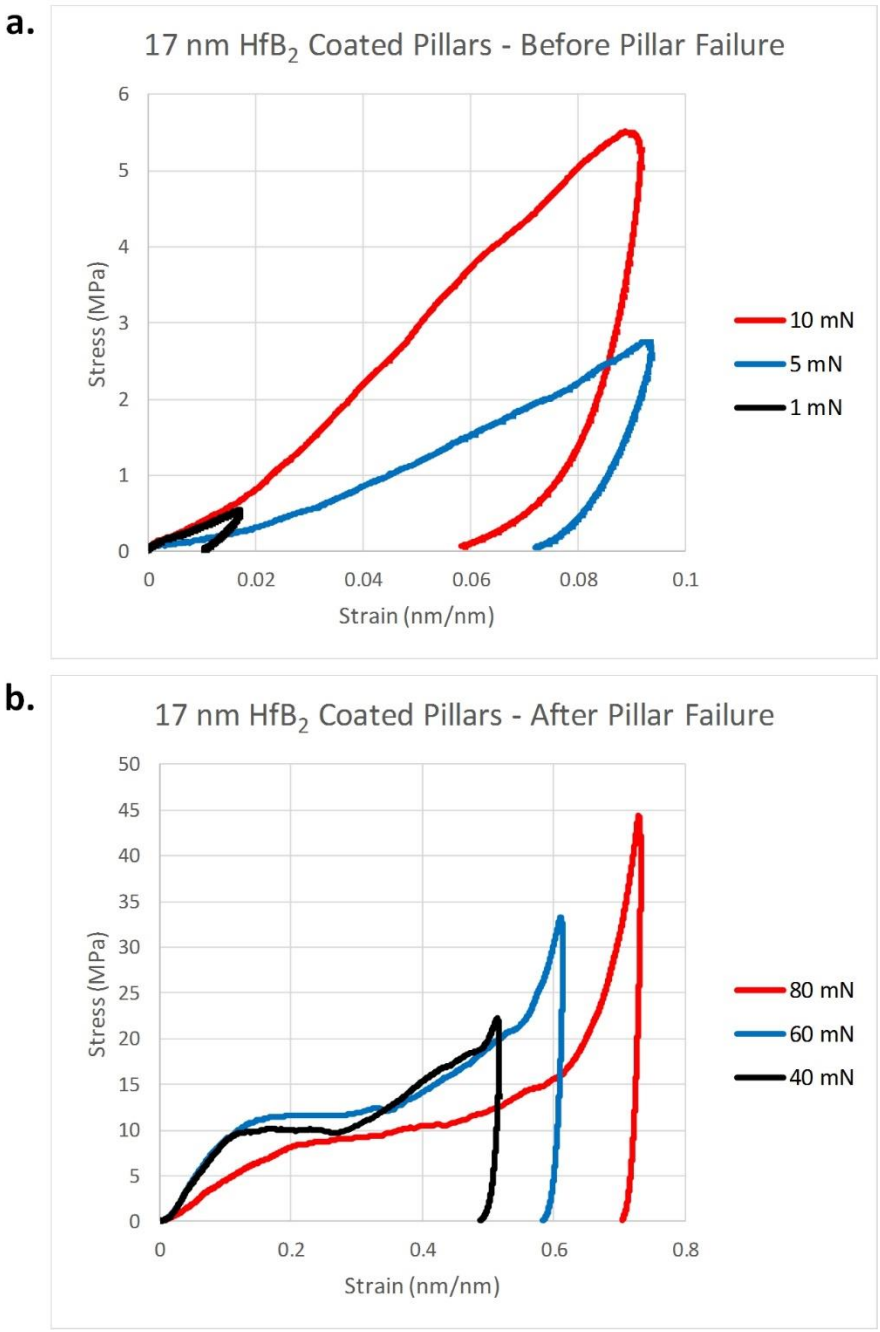

Figure 4.9 Stress-strain curves for the 17 nm HfB_2 coated CNT pillars a.) Data before pillar failure. b.) Data after pillar failure by fracture.

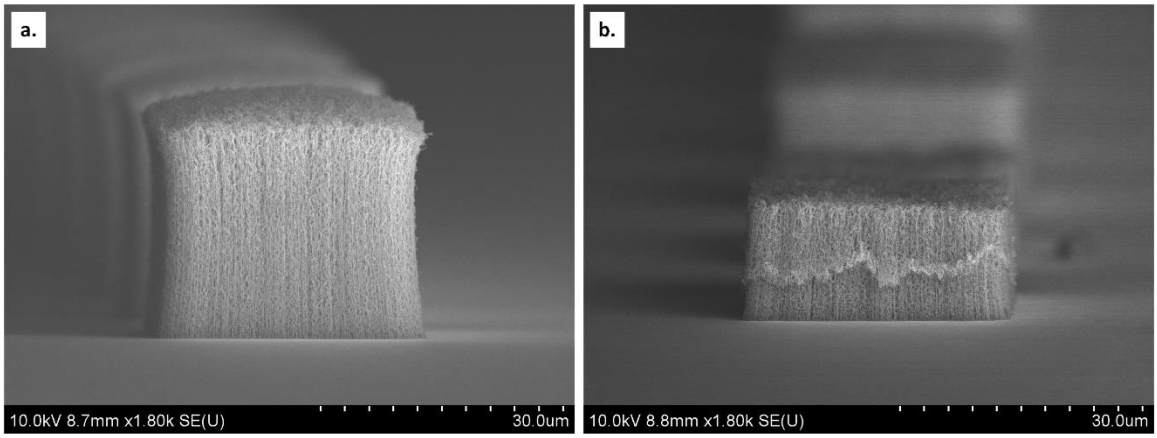

Figure 4.10 Tested 17 nm HfB2 coated CNT pillars. a.) Before pillar failure. b.) After pillar failure by fracture.

28 nm HfB_2 Coating Thickness

The stress values increase significantly for the 28 nm HfB_2 coated pillars to 45 MPa for stress before failure and approximately to 50 MPa for pillar failure (Figure 4.11 a.). In Figure 4.12 we see the behavior is very brittle and in Figure 4.13 a cracking phenomenon is observed. Since this cracking was only observed in the 28nm coating it is assumed that residual stresses caused the coating to break and fracture.

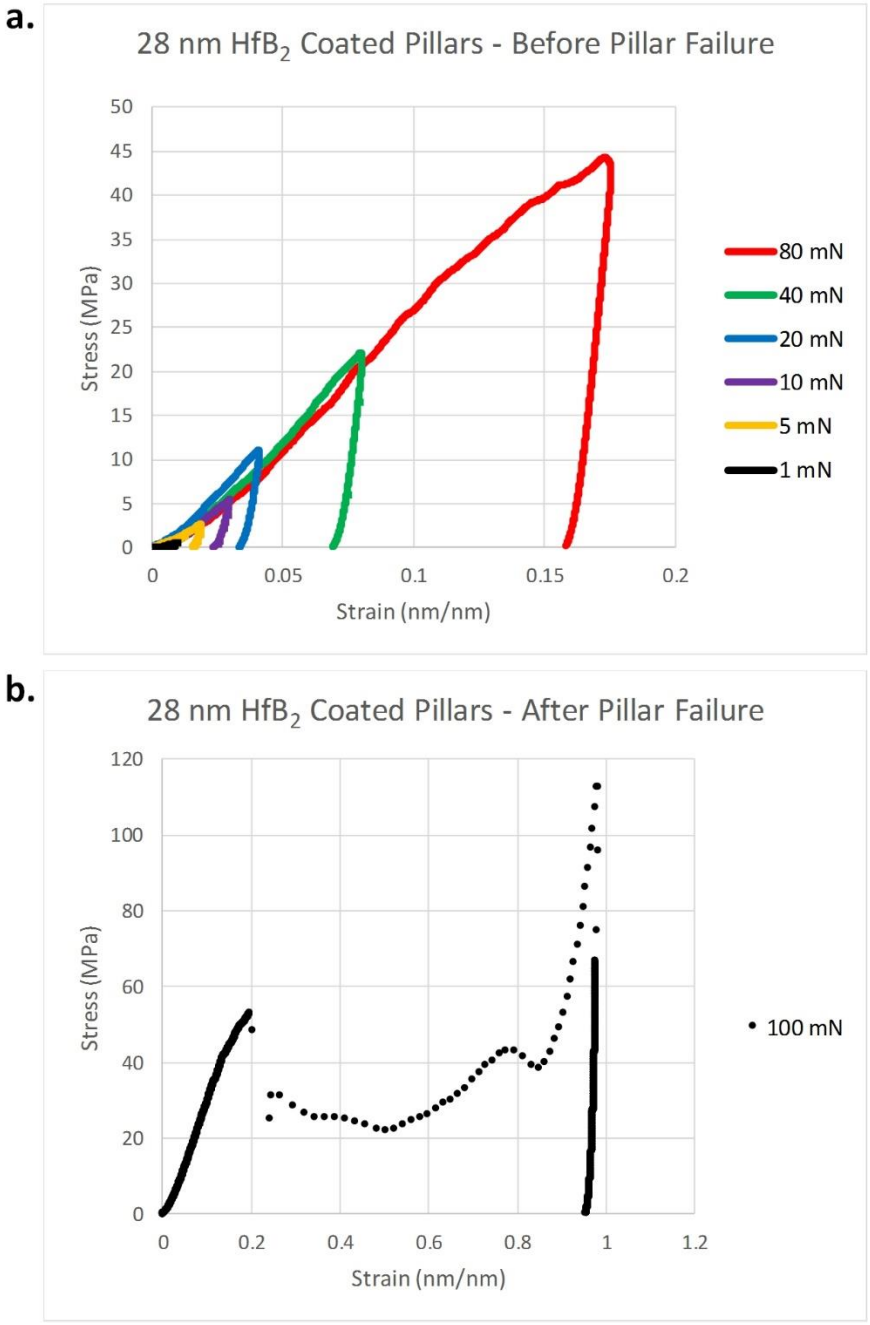

Figure 4.11 Stress-strain curves for the 28 nm HfB_2 coated CNT pillars a.) Data before pillar failure. b.) Data for damaged pillars from fracturing behavior.

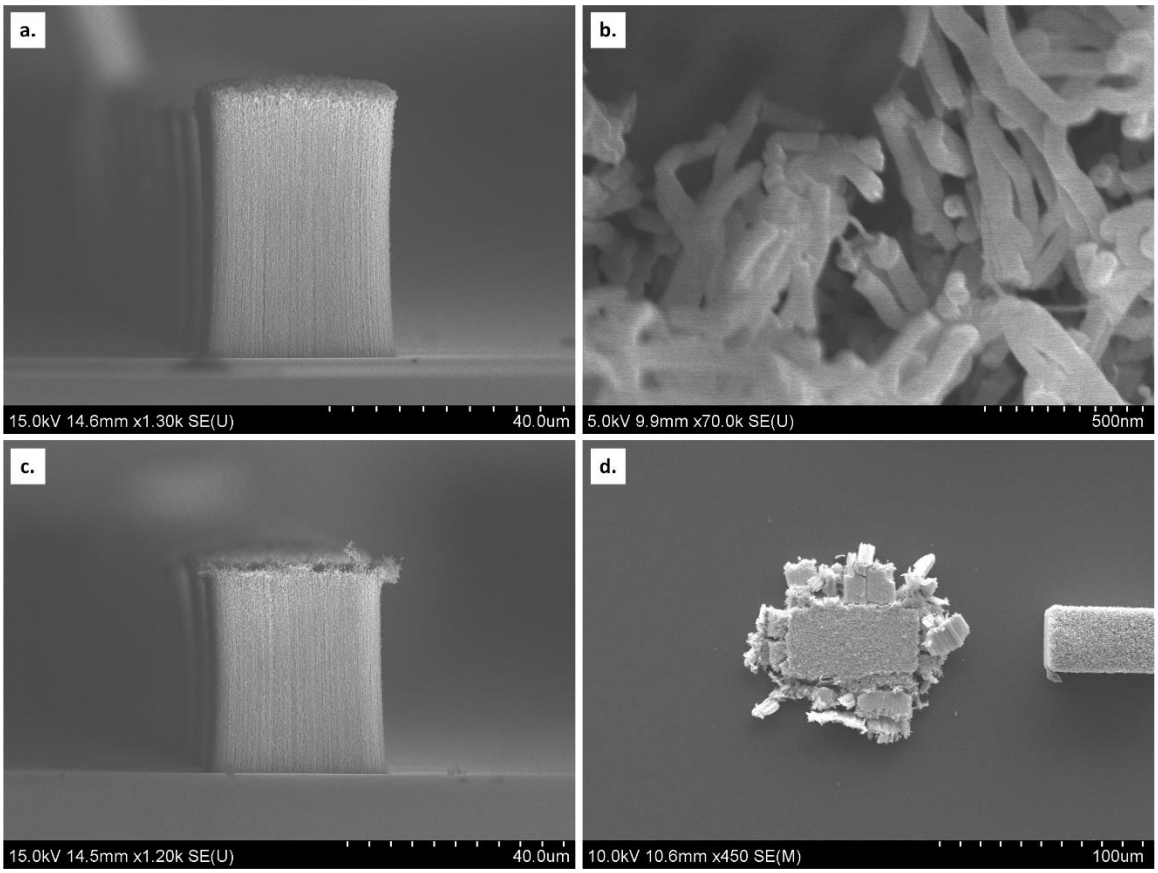

Figure 4.12 Tested 28 nm HfB2 coated CNT pillars. a.) Before pillar failure. b.) Coated CNTs depicting fractured coating. c.) Pillar failure by fracture. d.). Pillar showing very brittle behavior.

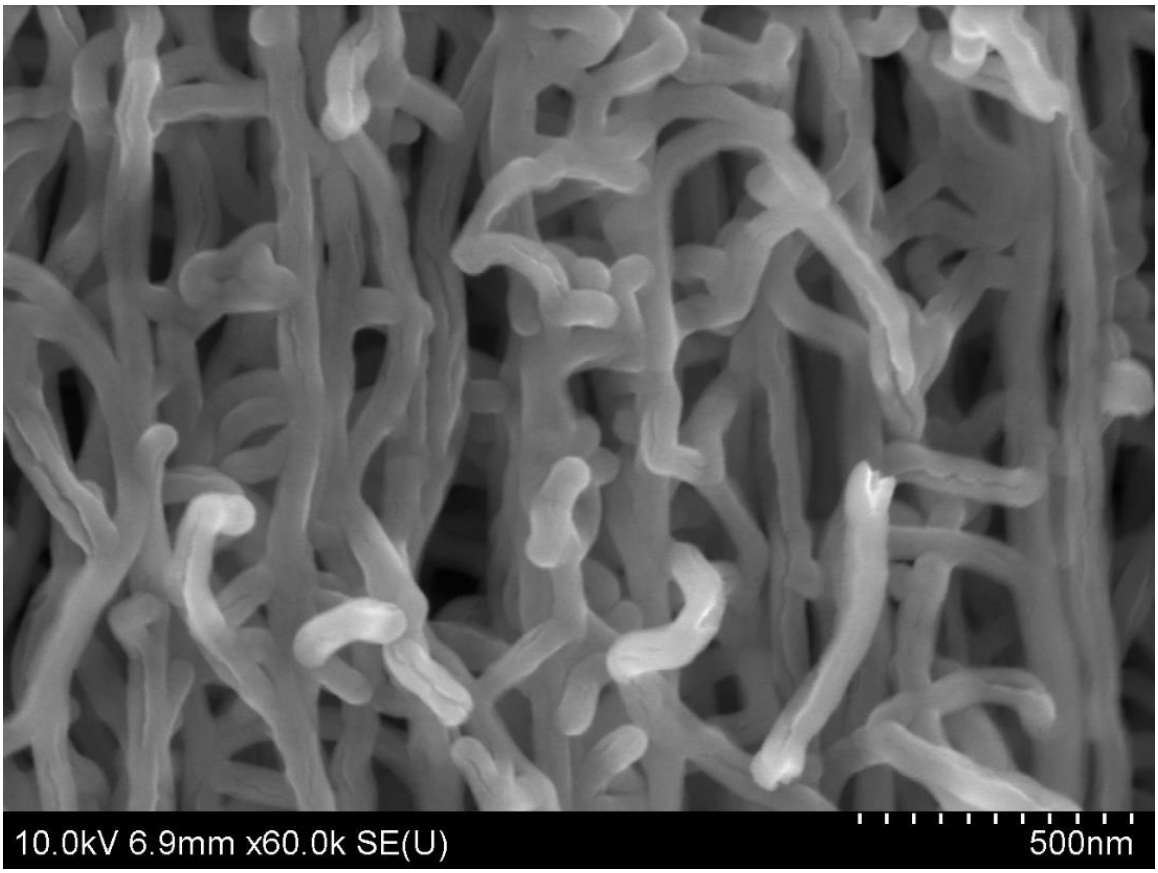

Figure 4.13 A cracking phenomenon can be seen on the CNT surfaces for the 28 nm coating.

50nm HfB_2 Coating Thickness

The final coating tested for the HfB_2 pillars was fully coalesced with no visible porosity as seen in Figure 4.15 a. This thickness was estimated to be 50 nm from known CNT "cell" size and past literature results. The stress-strain behavior is qualitatively different in this case. The quasi-elastic loading curve is non-linear with power higher than one as demonstrated by its upward concave shape. Also, the hysteresis is much lower, and most of the stress-strain is recovered. Using small diameter pillars, I was able to test the pillars until failure without saturating the indenter's load transducer.

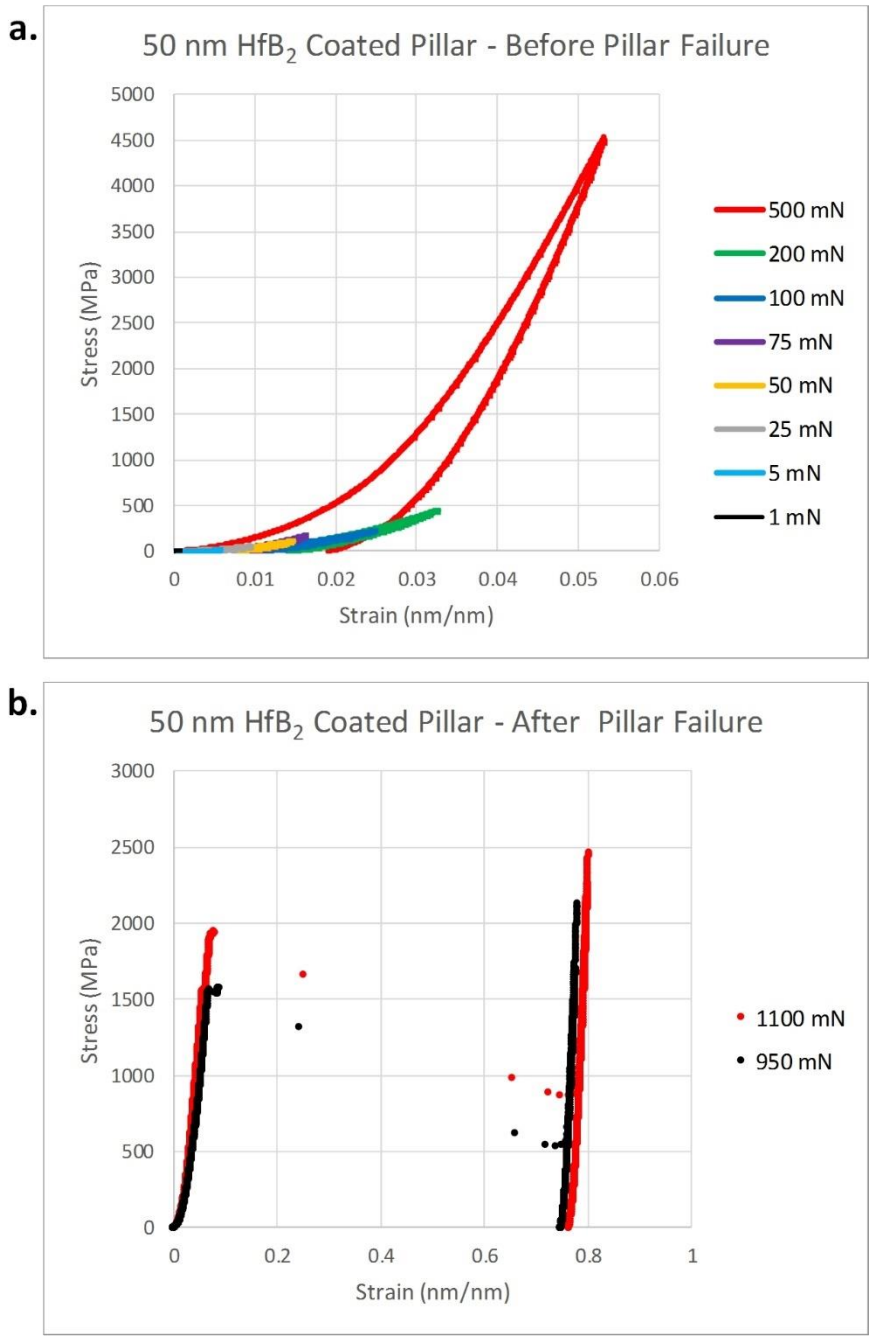

Figure 4.14 Stress-strain curves for coalesced HfB_2 coated CNT pillars. a.) Data before pillar failure. b.) Data after pillar failure by fracture.

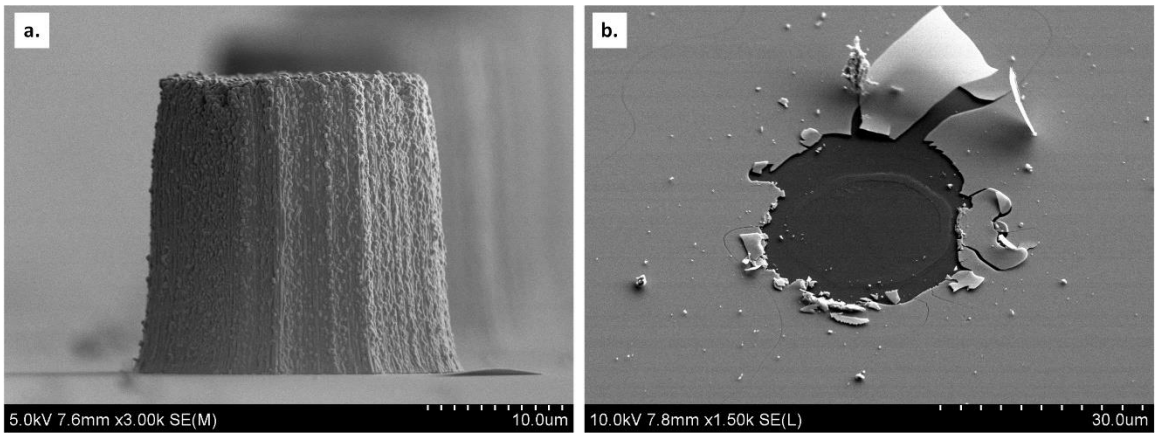

Figure 4.15 a.) The coalesced pillars were estimated to have a 50 nm coating thickness. b.) When the pillars were loaded till failure, they adhered to the tip.

4.4. Stress-Strain Plots for PDC Pillars

Two polymer derived ceramic (PDC) samples, one of short pillars and one of tall pillars, were created and tested. The first figures show the results of the short pillar sample (6.5 μm height), and the second figures show the results of the tall pillar sample (32 μm height). Each sample went through three cycles of PDC which consisted of spin coating the silicon oxycarbide (SiOC) solution over the pillars and high temperature pyrolysis. The pillars were found to shrink to an average final diameter of 32% of the original pillar diameter. The exact coating thickness could not be determined using the SEM due to charging. Attempts to coat the samples with thin gold for imaging didn't lead to much improvement in image quality.

PDC Cycle 1

The stress of the first cycle reaches up to 4MPa for the short pillars (Figure 4.18) and 1.2 MPa for the tall pillars (Figure 4.19 a.). This is much higher than the 0.16 MPa reported for the uncoated pillars from section 4.2. The short PDC pillars did not exhibit any failure behavior in nanoindentation testing. Therefore, only the tall pillar PDC sample was used to determine strength. The measured strength reached about 0.75 MPa.

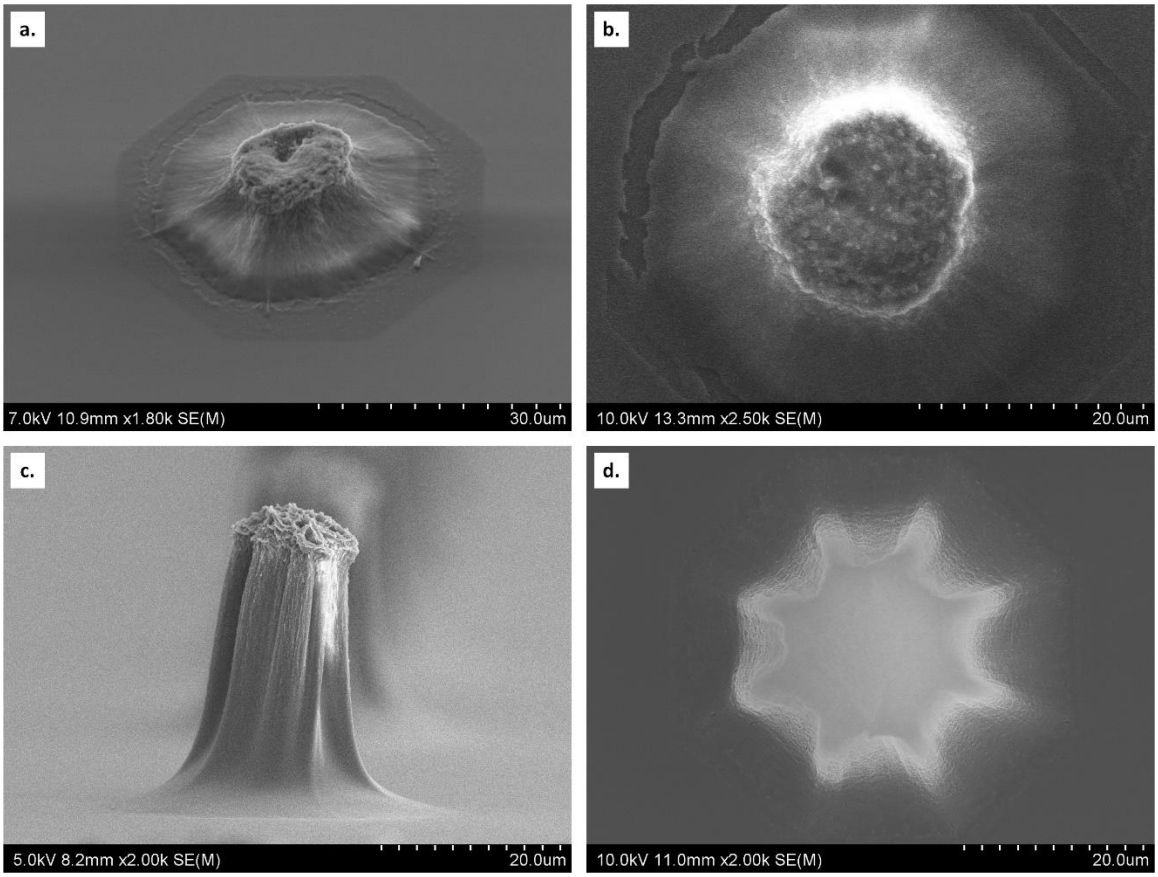

Figure 4.16. Untested pillars from one cycle of PDC. a-b.) The outline of the CNT catalyst can be seen in the short pillar sample. The pillar has shrunk in both diameter and height. c-d.) The tall pillar shrunk as well and has a more complex geometry.

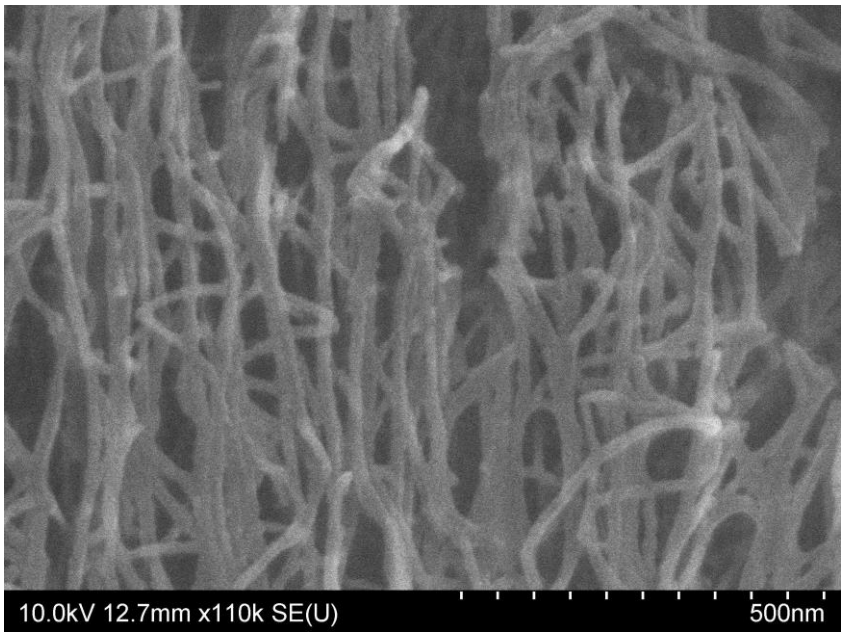

Figure 4.17 The average coating thickness from one cycle of PDC was approximately 8 nm.

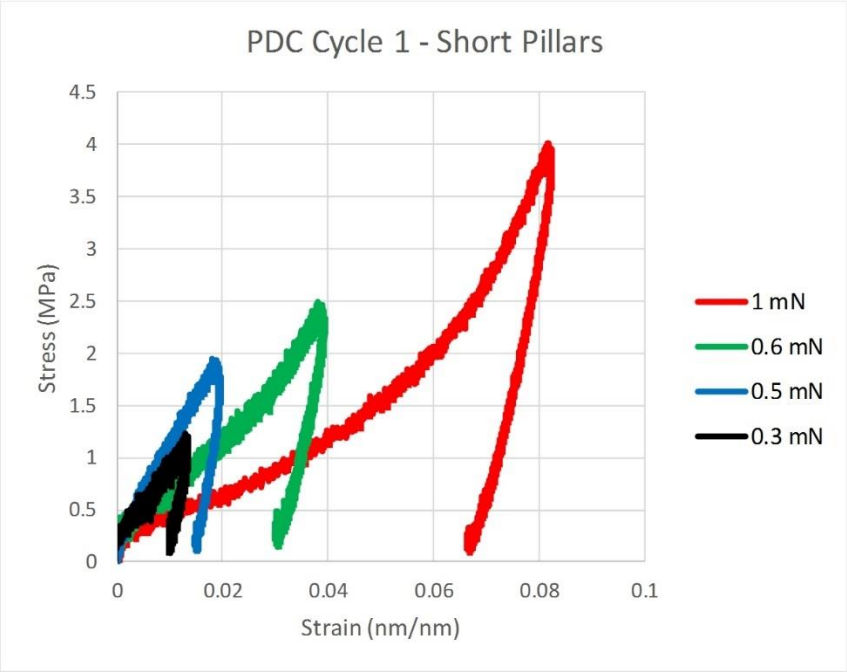

Figure 4.18 Stress-strain curves for the short CNT pillars with one PDC coating cycle.

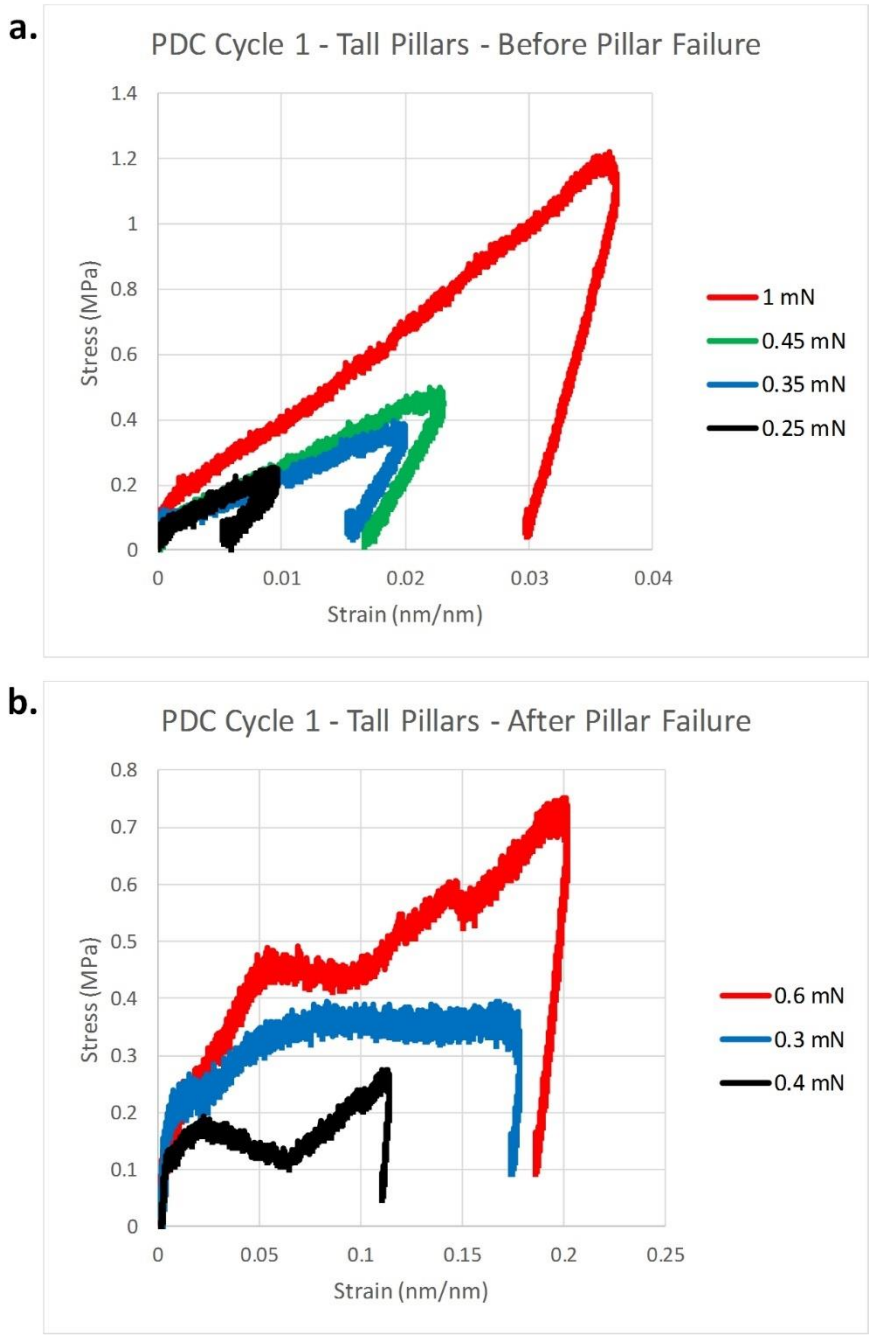

Figure 4.19 Stress-strain curves for the tall PDC pillars with one PDC coating cycle. a.) Data before pillar failure. b.) Data after pillar failure by fracture.

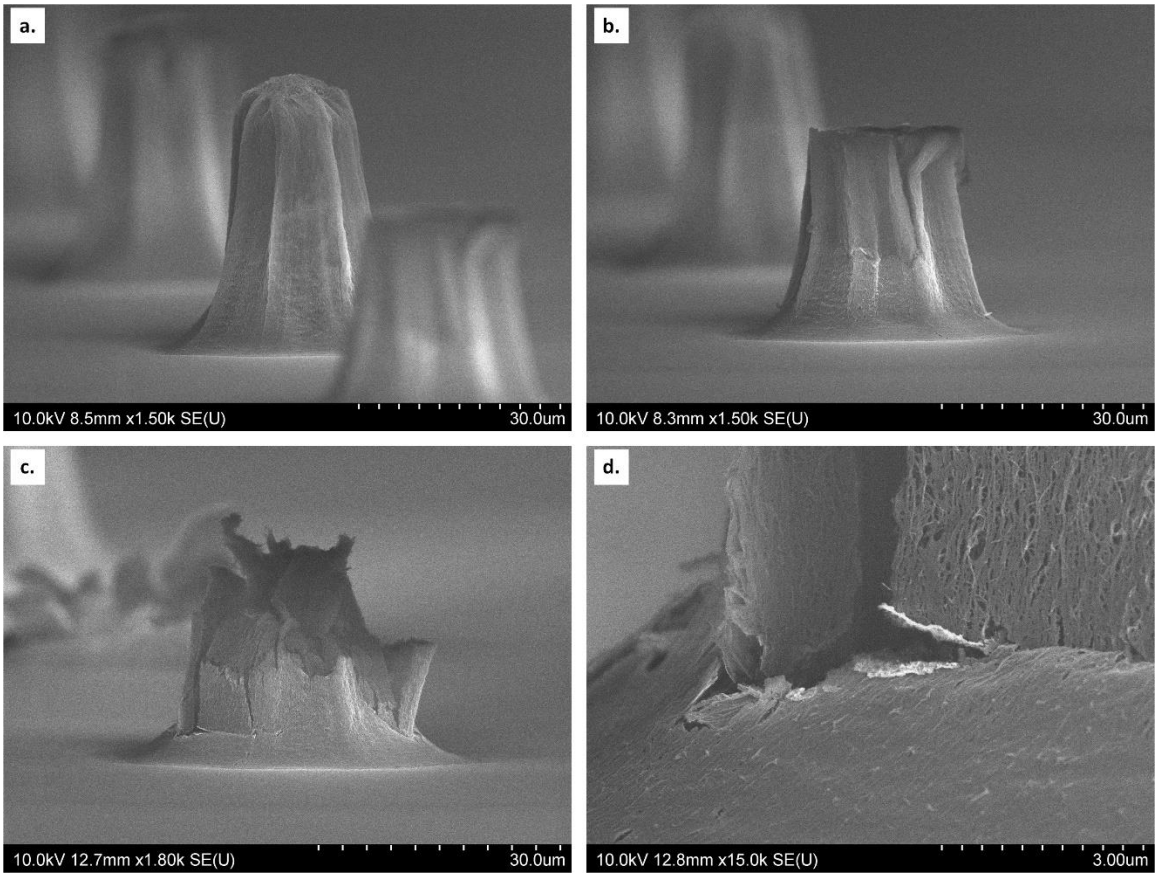

Figure 4.20 Tested tall PDC pillars. a.) Before pillar failure. b-c.) Fractured pillars d.) View showing brittle behavior at the base of the pillar.

PDC Cycle 2

The stress of the second cycle reached up to 20 MPa for the short pillars (Figure 4.21) and 6.5 MPa for the tall pillars (Figure 4.22 a.) before pillar failure which is about 5 times higher than the first cycle for both samples. The measured strength of the tall pillars reached about 9 MPa, up 12 times from the first cycle.

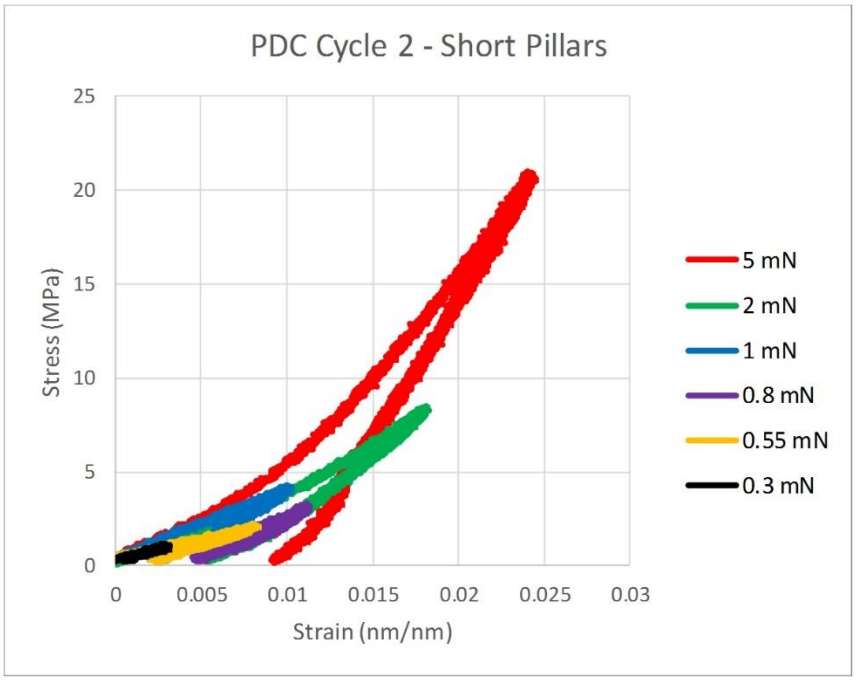

Figure 4.21 Stress-strain curves for the short CNT pillars with two PDC coating cycles.

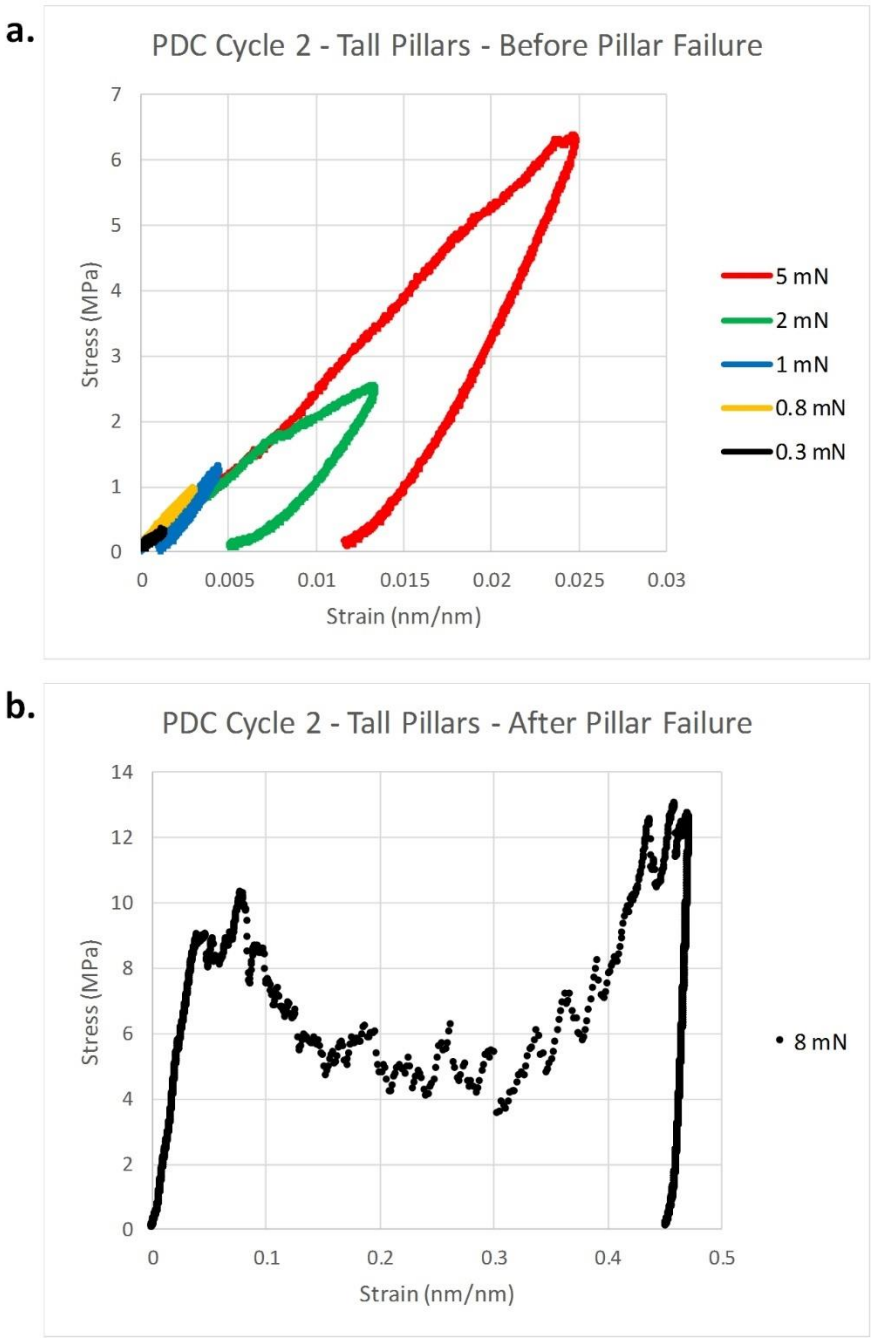

Figure 4.22 Stress-strain curves for the tall PDC pillars with two PDC coating cycles. a.) Data before pillar failure. b.) Data after pillar failure by fracture.

PDC Cycle 3

The stress of the third cycle reached 200 MPa for the short pillars (Figure 4.23) and about 13 MPa for the tall pillars (Figure 4.24 a.). This is a significant difference between the two samples. The short pillars increase 10 times while the tall pillars only double from the previous cycle (2 cycles). Since the short pillars do not exhibit failure, the indenter maybe getting a response from the silicon wafer as well. The measured strength of the tall pillars increased slightly from 9 MPa to 14 MPa.

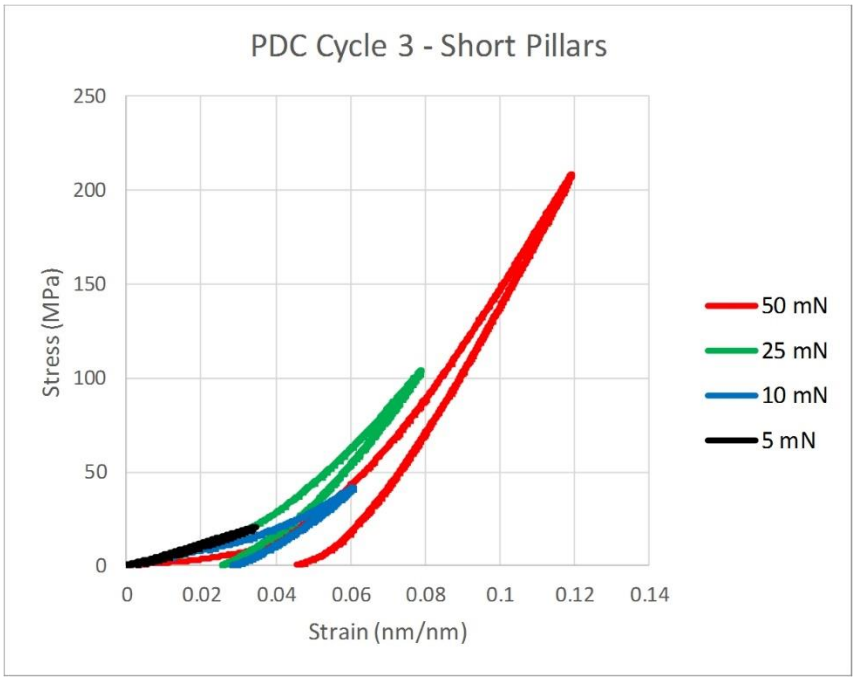

Figure 4.23 Stress-strain curves for the short CNT pillars with three PDC coating cycles.

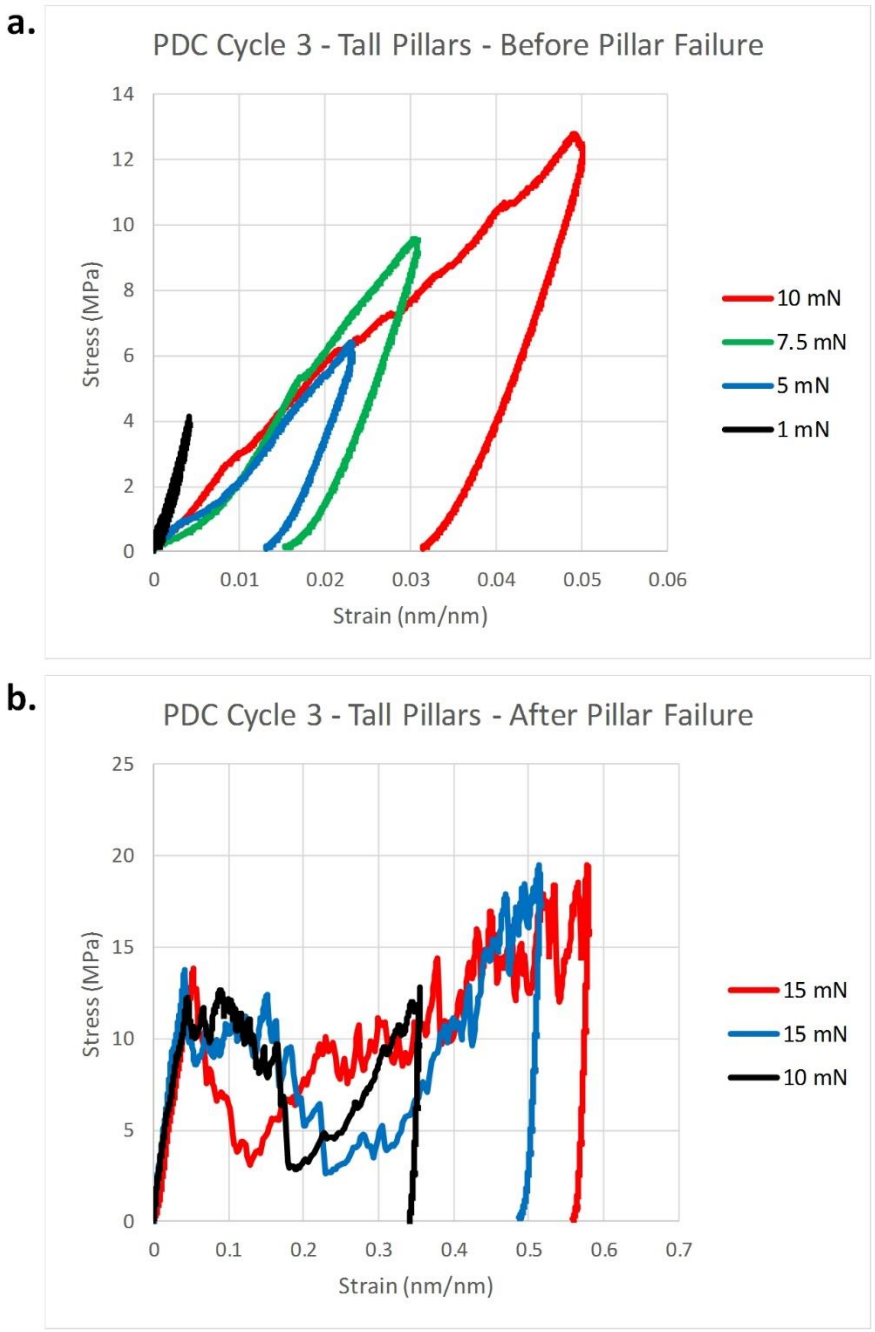

Figure 4.24 Stress-strain curves for the tall PDC pillars with three PDC coating cycles. a.) Data before pillar failure. b.) Data after pillar failure by fracture.

CHAPTER 5: DISCUSSION

5.1. Introduction

The nanoindentation testing results can provide more information about the properties of carbon nanotube CNT composites beyond the stress-strain curves. Slopes were extracted from the unloading portion of the curves and used to measure the Young's modulus. The Young's modulus can then be plotted as a function of coating thickness for the various thicknesses of the hafnium diboride (HfB_2) and the polymer derived ceramic (PDC) coated pillars. The maximum stress before failure was also averaged and plotted as a function of coating thickness.

5.2. Young's Modulus as a Function of Coating Thickness

The Young's modulus is extracted from the slope of the stress-strain curve. It is important to note that pillar behavior and the shape of the stress-strain curve varied with thickness. This affected the loading and unloading regimes observed. For example, in some stress-strain curves there are two distinct slopes observed. However, other curves have up to four slopes as shown in Figure 5.1. This disparity could be related to how coating thickness affects pillars under compression, a variation of the nanoindentation testing, or a combination of the two. The first region is the loading portion. The loading slope begins once the tip has contacted the pillar (after the initial pre-load of the load function) and begins compressing the material to the desired load. Some curves exhibit an initial slope after the pre-load but before the loading contributing to multiple slopes. One explanation for this could be that the pre-load already compressed the top of the pillar. There could also be something on the tip. The second typical region is the unloading portion when the tip is removed from the pillar. In most cases the unloading region is not linear. The unloading slope is the slope that was used to extract the Young's modulus.

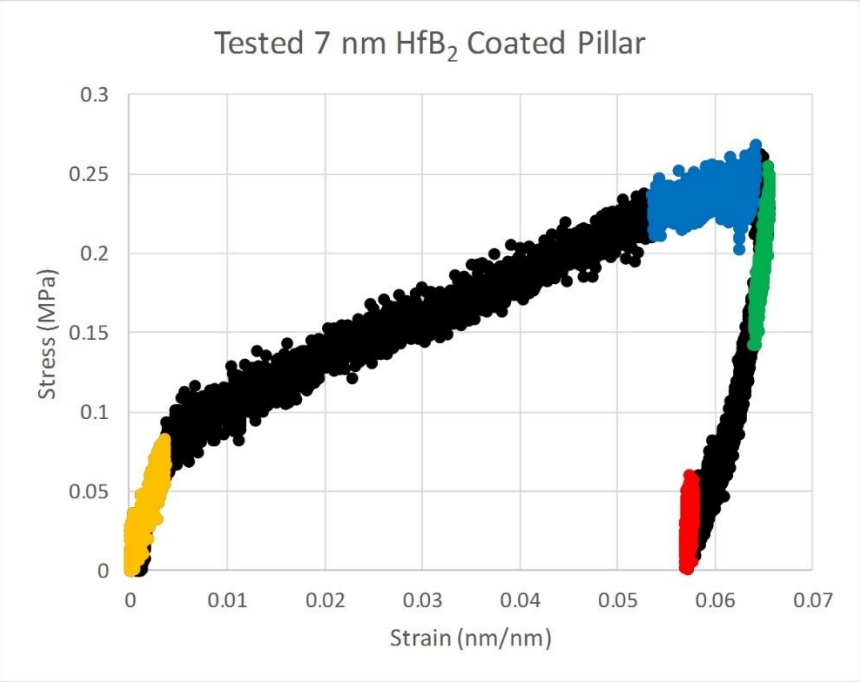

Figure 5.1 Stress-strain curve showing four distinct slopes within the loading and unloading regimes.

Unloading Slope

The Young's modulus was only extracted from the unloading slopes of the stress-strain curves before pillar failure. Buckled or failed pillars were not included in the data. It is challenging to depict when the elastic response transforms into the plastic response and thus the loading slope in unreliable for measuring an elastic modulus. Oliver et al. [15] shows that it is acceptable to use the unloading slope for the Young's modulus measurements.

Figure 5.2 demonstrates the slope extraction for a coalesced pillar of HfB_2. The range of the strain for the unloading region was found and the first 10% of this region (unloading the tip from the pillar) was used to calculate the slope. I found the maximum and the minimum strain values of the unloading region and determined what 10% of this range is. Then, the maximum strain value can be used to determine the first 10% of the unloading region. The HfB_2 Young's modulus is presented in Figure 5.3 and the polymer derived ceramic modulus is presented in Figure 5.5. The unloading slope increases slightly with the maximum stress reached before unloading. I found that it is important to be consistent and very clear in defining how the Young's modulus is obtained.

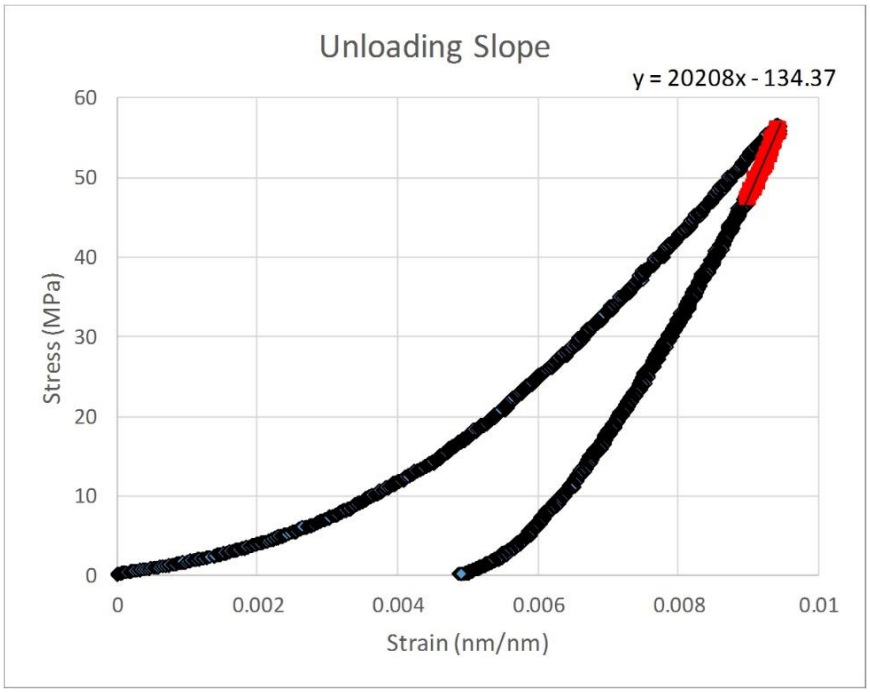

Figure 5.2 Unloading slope extraction from the first 10% of the unloading region of a HfB_2 coated pillar.

Hafnium Diboride Young's Modulus

The Young's modulus for HfB_2 as a function of coating thickness is shown Figure 5.3. The x-axis is coating thickness in nanometers and the y-axis is a log scale of the Young's Modulus in megapascals. The data shows a linear trend. The values plotted are taken from the results presented in Chapter 4. A linear trend is noted with increasing thickness. The Young's modulus increases from 12.01 MPa for uncoated pillars to 56.49 GPa for approximately 50 nm coated HfB_2 pillars. This is a ~4700 fold increase in Young's modulus. For each thickness, the variation in the value of moduli can be correlated to the maximum stress for this test before unloading. The highest modulus value for a given thickness usually corresponds to the pillar tested at the highest possible stress value before collapse.

The Young's modulus was plotted against density to determine a power law relationship (Figure 5.4). The relationship was determined to be $E \sim \rho^{1.698}$. Density was found using a CNT cell size of 115 nm with an outer radii of 5 nm and inner radii of 3 nm. The density used for CNTs was 2,200 kg/m^3 and the density used for HfB_2 was 10,500 kg/m^3.

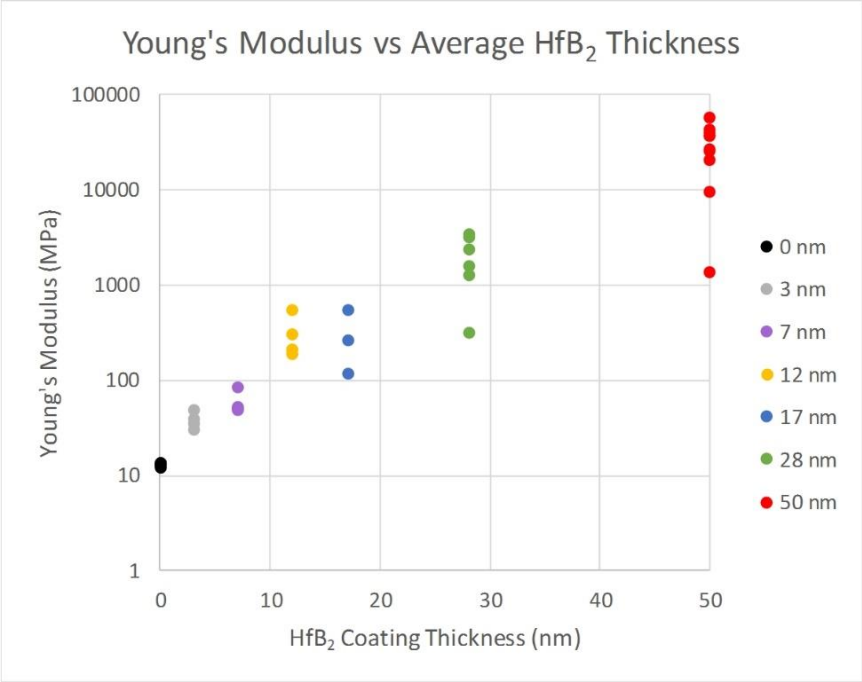

Figure 5.3 The Young's modulus is derived from the unloading slopes of the stress-strain curves for uncoated and HfB_2 coated pillars before pillar failure.

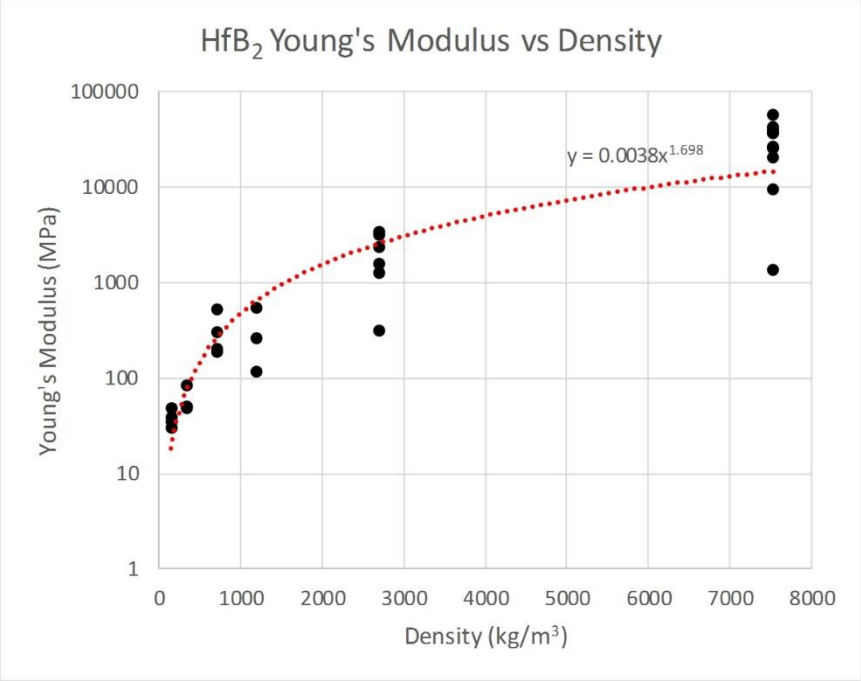

Figure 5.4 Young's modulus as a function of density for HfB_2 coated pillars before pillar failure.

Polymer Derived Ceramic Young's Modulus

The PDC samples also see a significant increase in Young's Modulus from 12.01 MPa to 3.80 GPa resulting in ~300 fold increase. The short pillars sample had a significantly higher Young's modulus than the tall pillars (Figure 5.5).

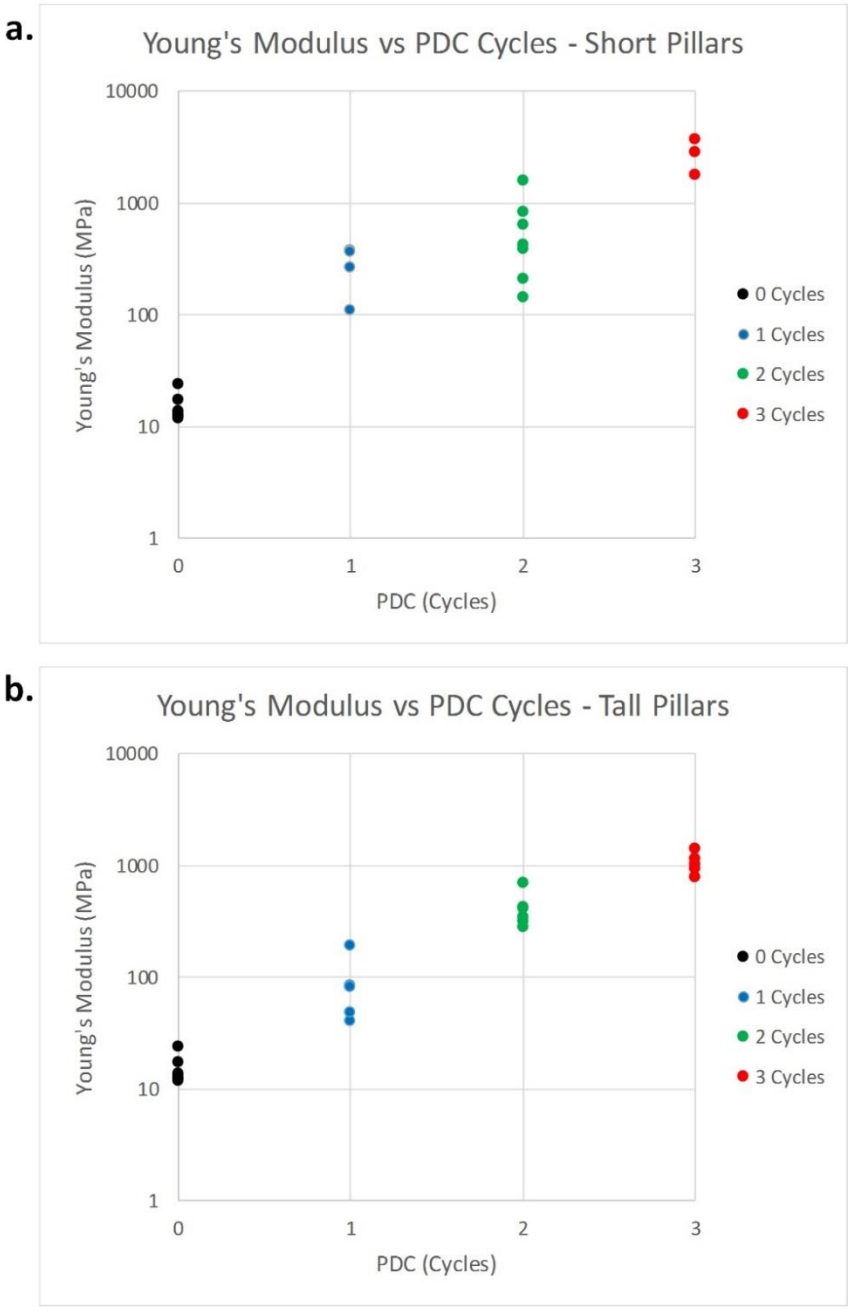

Figure 5.5 The Young's modulus is derived from the unloading slopes of the stress-strain curves for uncoated and PDC coated pillars before pillar failure. a.) The data for the short pillar sample. b.) The data for the tall pillar sample.

5.3. Strength as a Function of Coating Thickness

The stress-strain curves reported in Chapter 4. The maximum buckling stress for each set of failed pillars by either collapse or fracture was averaged and is reported in Figure 5.6 for HfB_2 coated pillars and Figure 5.7 for PDC pillars. Figure 5.8 shows an example of how the strength value was determined. The highest stress value before the pillar exhibited failure on the stress-strain curves of the after pillar failure plots was averaged and used as the reported strength. For HfB_2 coated pillars the highest strength was 1.94 GPa for approximately 50 nm coated pillars. For the PDC pillars it was 13.87 MPa.

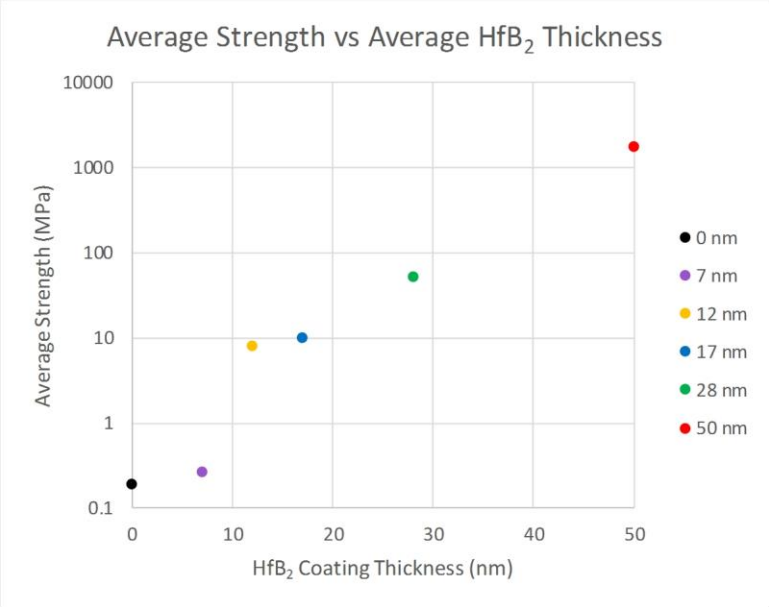

Figure 5.6 The average compressive strength for uncoated and HfB_2 coated pillars.

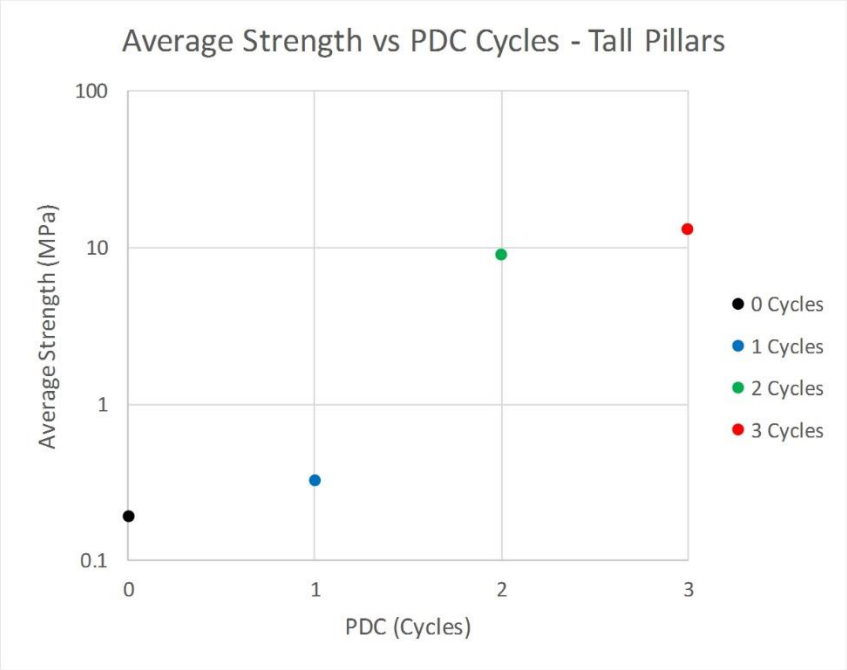

Figure 5.7 The average compressive strength for uncoated and SiOC coated pillars.

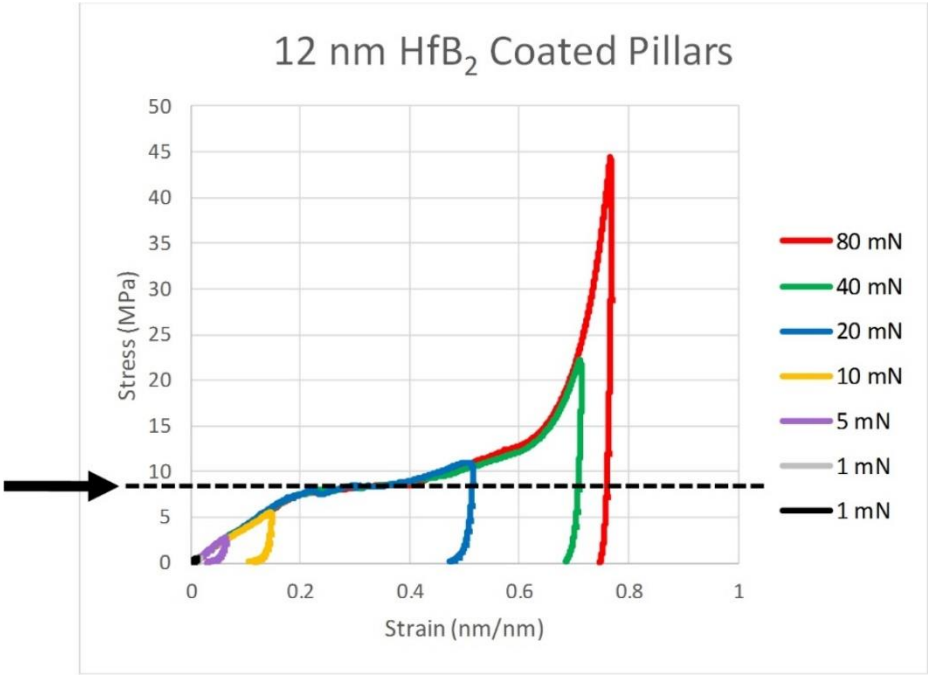

Figure 5.8 The arrow indicated the maximum stress of the 12nm HfB2 coated pillars before failure.

CHAPTER 6: CONCLUSIONS AND RECOMMENDATIONS

6.1. Overview

The purpose of this study was to create and test carbon nanotube (CNT) composite foams to investigate their mechanical properties and to better understand the coating procedures of high temperature ceramics. Chemical vapor deposition (CVD) and spin-coating allowed for the coating materials to infiltrate and coat the porous nanostructure of the CNT pillars. A wide range of thicknesses were used to characterize the pillars with two different high temperature ceramics. Hafnium diboride (HfB_2) is an ultra-high ceramic material that was coated using CVD and SiOC was coated as a PDC coating using spin-coating and pyrolysis. The pillars were tested using nanoindentation and the load-displacement curves were used to determine the Young's modulus and buckling stress of the CNT composite foams. Scanning electron microscopy (SEM) was conducted on tested pillars to further characterize their behavior and properties.

6.2. Conclusions

From this study, the following conclusions were drawn:

Coating Methods

1. The size of the CNT forest within a sample (i.e. CNT micropillar) is significant during static-CVD coating because of the amount of CNT surface area. The rate at which the precursor gases are used varies based on the precursor pressure and sample size. The final coating thickness can be determined using high resolution SEM.
2. For a large thickness of 28 nm HfB_2 coating, a cracking phenomenon was observed. This cracking may have been due to residual stresses because of the CVD process.
3. The PDC coated CNT pillars were found to shrink to a final diameter of 32% of the original pillar diameter.
4. PDC can be used to coat and infiltrate the inner pores of a CNT pillar. However, the initial cycle of PDC coalesces on the outside of the CNT pillar. As a result, I expect that the interior remains somewhat porous. Continued cycles of PDC improve the CNT pillar properties but are no longer able to infiltrate the pillar.

Compression Testing Protocol

1. I was not able to get reliable measurements with displacement control load functions. The pillars collapsed before the load function could reach the desired displacement. I used load control for all the tests presented in this thesis.
2. Tip compatibility is important. The Hystiron instrument used in this study can function with a low-load or high-load transducer. However, the flat-punch diamond tip used in these experiments was only compatible with the high-load transducer. Compatibility with the low-load transducer would have been useful for testing uncoated and thinly coated CNT pillars.
3. Nanoindentation presents challenges for uncoated CNT pillars of small diameters. The pillars adhered to the tip and were stripped from the silicon surface. To overcome this challenge, the tip or the pillars can be sputtered with a thin layer of gold. Double-sided tape can be used to remove the pillar from the tip.
4. The high-load transducer on the nanoindenter reached its load limit when testing coalesced pillars of HfB_2 with large diameters (>25 μm). However, the indenter was able to damage smaller diameter pillars.

Reported Properties

1. The highest stiffness for uncoated pillars was 12.01 MPa.
2. The highest stiffness for HfB_2 coated pillars was 56.49 GPa for approximately 50 nm coated pillars.
3. The trend in stiffness for the HfB_2 coated pillars was $E \sim \rho^{1.698}$.
4. The highest stiffness for SiOC coated pillars was 3.80 GPa for 3 cycles of PDC pyrolysis.
5. The highest strength for HfB_2 coated pillars was 1.94 GPa for approximately 50 nm coated pillars.
6. The highest strength for SiOC coated pillars was 13.87 MPa for 3 cycles of PDC pyrolysis.

6.3. Recommendations for Future Work

I recommend several steps to improve this study to better understand the coatings of HfB_2 and SiOC and to better understand how the CNT composite foams behave. A large array of HfB_2 thicknesses were tested in this study. However, the impact of coating thickness over the CNT elements and CNT junctions was not explored. A model to represent this would better explain how thickness correlates to the mechanical behavior.

For the SiOC coated PDC samples, studying how the solution infiltrates the CNT pillars is important to understanding how much of the pillar is coated. I also recommend additional cycles and SEM images for each cycle to find a trend in the stiffness.

Recommended Steps

1. In the 28 nm HfB_2 coating, a cracking phenomenon was observed on the individual CNTs. It was suggested that this phenomenon could be due to residual stresses of the coating during the CVD process. It is important to further investigate when this cracking forms and how it affects localized coating of the CNTs.
2. A fiber pull-out phenomenon was observed in the HfB_2 coating of some samples. This was primarily observed after nanoindentation and could be a result of localized fracture of the CNT coating. I recommend studying what causes CNT fiber pull-out and if there is adhesion between the coating and the CNTs.
3. For PDC work, I suggest that the surface angle between PDC and CNT should be measured to determine its ability to infiltrate the CNTs.

REFERENCES

[1] U. G. K. Wegst *et al.*, "Bioinspired structural materials," *Nat. Mater.*, vol. 14, no. 1, pp. 23–36, 2014.

[2] A. Brieland-Shoultz *et al.*, "Scaling the Stiffness, Strength, and Toughness of Ceramic-Coated Nanotube Foams into the Structural Regime," *Adv. Funct. Mater.*, vol. 24, no. 36, pp. 5728–5735, 2014.

[3] F. Bouville, E. Maire, S. Meille, B. Van de Moortèle, A. J. A. J. Stevenson, and S. Deville, "Strong, tough and stiff bioinspired ceramics from brittle constituents.," *Nat. Mater.*, vol. 13, no. 5, pp. 508–14, 2014.

[4] H. Le Ferrand, F. Bouville, T. P. Niebel, and A. R. Studart, "Magnetically assisted slip casting of bioinspired heterogeneous composites," *Nat. Mater.*, vol. 14, no. September, pp. 1–17, 2015.

[5] L. J. Bonderer, "Bioinspired Design and Assembly of Platelet Reinforced Polymer Films," *Science (80-.).*, vol. 205411, no. 2003, pp. 1069–1073, 2007.

[6] R. H. Poelma *et al.*, "Tailoring the mechanical properties of high-aspect-ratio carbon nanotube arrays using amorphous silicon carbide coatings," *Adv. Funct. Mater.*, vol. 24, no. 36, pp. 5737–5744, 2014.

[7] W. G. Fahrenholtz, G. E. Hilmas, I. G. Talmy, and J. A. Zaykoski, "Refractory diborides of zirconium and hafnium," *J. Am. Ceram. Soc.*, vol. 90, no. 5, pp. 1347–1364, 2007.

[8] R. Loehman, E. Corral, H. Dumm, P. Kotula, and R. Tandon, "Ultra high temperature ceramics for hypersonic vehicle applications.," no. June, p. 46, 2006.

[9] D. Marshall, *National Hypersonic Science Center for Materials and Structures Materials and Structures for Propulsion Flowpath*, vol. 298, no. 704. 2011.

[10] Z. C. Eckel, C. Zhou, J. H. Martin, A. J. Jacobsen, W. B. Carter, and T. A. Schaedler, "Additive manufacturing of polymer-derived ceramics.," *Science*, vol. 351, no. 6268, pp. 58–62, 2016.

[11] R. H. Poelma, X. Fan, Z. Y. Hu, G. Van Tendeloo, H. W. Van Zeijl, and G. Q. Zhang, "Effects of Nanostructure and Coating on the Mechanics of Carbon Nanotube Arrays," *Adv. Funct. Mater.*, 2016.

[12] P. P. S. S. Abadi, M. R. Maschmann, J. W. Baur, S. Graham, and B. a Cola, "Deformation response of conformally coated carbon nanotube forest.," *Nanotechnology*, vol. 24, no. 47, p. 475707, 2013.

[13] P. Pour, S. S. Abadi, M. R. Maschmann, J. W. Baur, S. Graham, and B. A. Cola, "Deformation response of conformally coated carbon nanotube forests," vol. 475707, 2013.

[14] A. Gallardo-López, R. Poyato, A. Morales-Rodríguez, A. Fernández-Serrano, A. Muñoz, and A.

Domínguez-Rodríguez, “Hardness and flexural strength of single-walled carbon nanotube/alumina composites,” *J. Mater. Sci.*, vol. 49, no. 20, pp. 7116–7123, 2014.

[15] W. C. Oliver and G. M. Pharr, “Measurement of hardness and elastic modulus by instrumented indentation: Advances in understanding and refinements to methodology,” *J. Mater. Res.*, vol. 19, no. 1, pp. 3–20, 2004.

[16] S. B. Hutchens, L. J. Hall, and J. R. Greer, “In situ mechanical testing reveals periodic buckle nucleation and propagation in carbon nanotube bundles,” *Adv. Funct. Mater.*, vol. 20, no. 14, pp. 2338–2346, 2010.

[17] a a Zbib, S. D. Mesarovic, E. T. Lilleodden, D. McClain, J. Jiao, and D. F. Bahr, “The coordinated buckling of carbon nanotube turfs under uniform compression.,” *Nanotechnology*, vol. 19, no. 17, p. 175704, 2008.

[18] S. R. Shah and R. Raj, “Nanodevices that explore the synergies between PDCs and carbon nanotubes,” *J. Eur. Ceram. Soc.*, vol. 25, no. 2–3 SPEC. ISS., pp. 243–249, 2005.

[19] Y. Cai, S. R. Shah, A. Zimmermann, M. Weinmann, R. Raj, and F. Aldinger, “Carbon nanotubes welded by precursor-derived silicoboron carbonitride ceramics: A TEM study,” *Phys. Status Solidi Appl. Res.*, vol. 193, no. 3, pp. 13–16, 2002.

[20] a. J. Kessman, J. Zhang, S. Vasudevan, J. Lou, and B. W. Sheldon, “Carbon Nanotube Pullout, Interfacial Properties, and Toughening in Ceramic Nanocomposites: Mechanistic Insights from Single Fiber Pullout Analysis,” *Adv. Mater. Interfaces*, vol. 2, no. 2, p. n/a-n/a, 2015.

APPENDIX A: STAGE TO TIP CALIBRATION

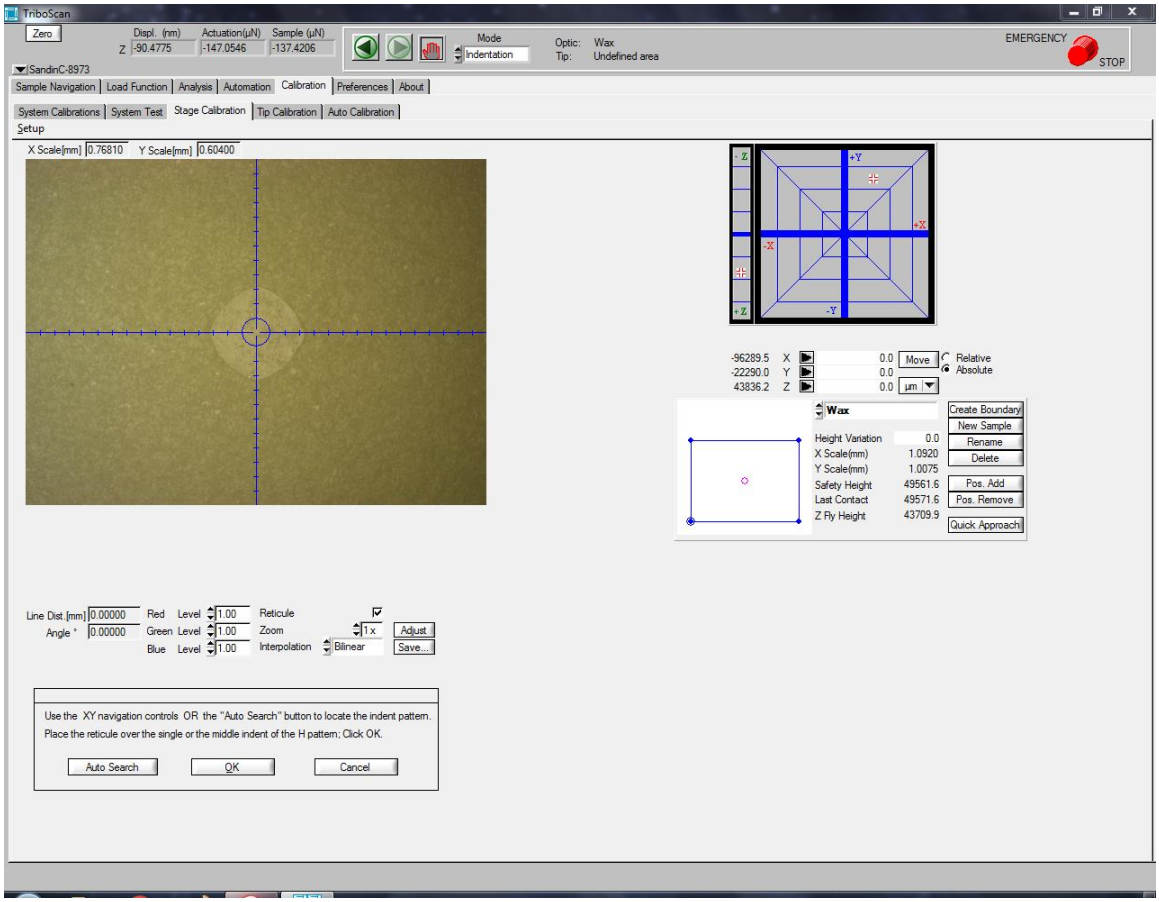

TriboScan calibration page. An indentation in a wax sample using a flat-punch tip.

APPENDIX B: SAMPLE NAVIGATION

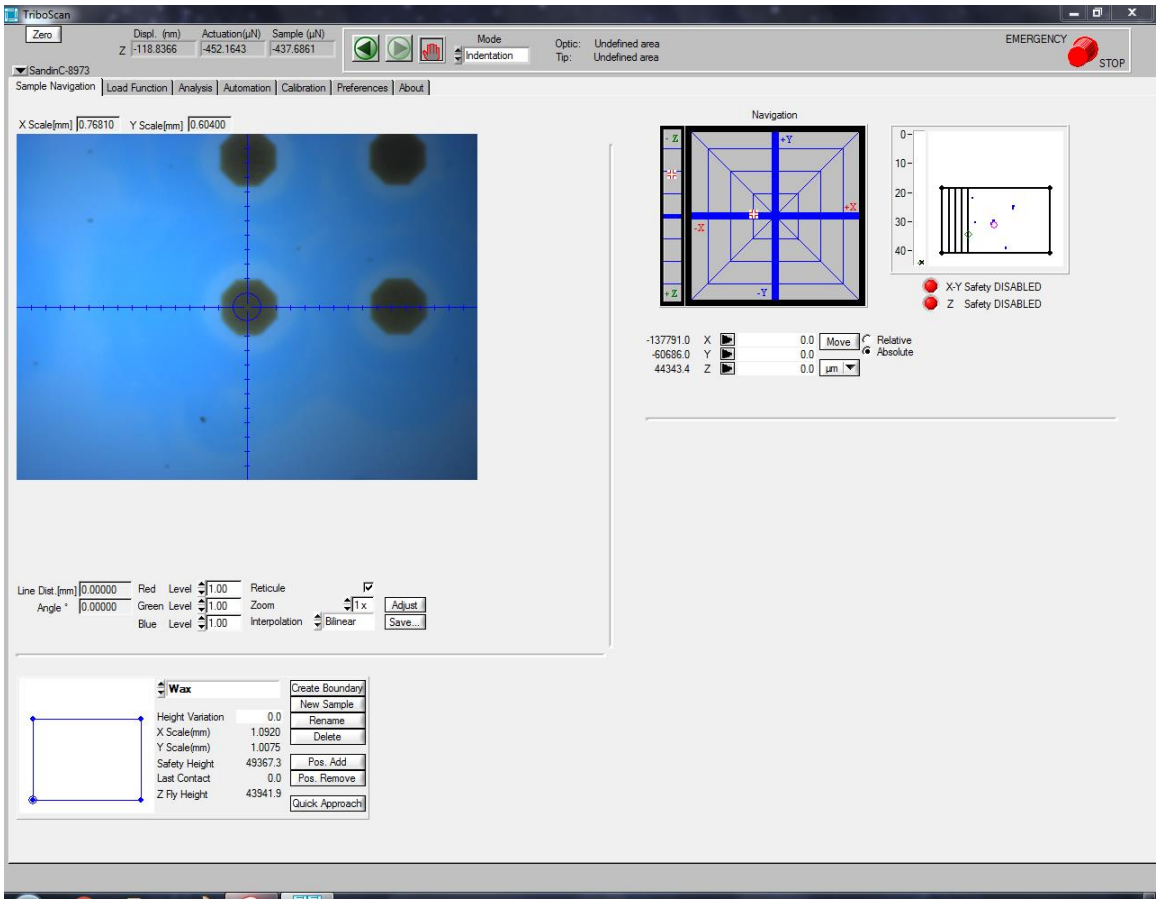

TriboScan sample navigation page. Each pillar was tested only once.